

THESIS FOR THE DEGREE OF DOCTOR OF PHILOSOPHY

**Numerical Investigations of
Turbulent Flow in
Water Turbines**

HÅKAN NILSSON

Department of Thermo and Fluid Dynamics

CHALMERS UNIVERSITY OF TECHNOLOGY

Göteborg, Sweden, 2002

Numerical Investigations of Turbulent Flow in Water Turbines
HÅKAN NILSSON
ISBN 91-7291-187-5

© HÅKAN NILSSON, 2002

Doktorsavhandlingar vid Chalmers tekniska högskola
Ny serie nr 1869
ISSN 0346-718X

Institutionen för termo- och fluidodynamik
Chalmers tekniska högskola
SE-412 96 Göteborg, Sweden
Phone +46-(0)31-7721400
Fax: +46-(0)31-180976

Cover:

The Hölleforsen Kaplan turbine model geometry. Excluded in the picture are the stay vanes, parts of the spiral casing and parts of the runner shroud.

Printed at Chalmers Reproservice
Göteborg, Sweden 2002

Numerical Investigations of Turbulent Flow in Water Turbines

by

HÅKAN NILSSON

Department of Thermo and Fluid Dynamics

Chalmers University of Technology

SE-412 96 Göteborg, Sweden

<http://www.tfd.chalmers.se/~hani>

Abstract

This thesis investigates turbulent flow in water turbines, focusing on the flow in the vicinity of reaction water turbine runners such as the Kaplan runner and the Francis runner. The method of investigation is principally numerical although some experimental observations and measurements made in the present work and elsewhere are included.

A major part of the present work was to implement an efficient and general CFD (Computational Fluid Dynamics) code that could resolve the complicated geometry of a water turbine. A parallel multiblock finite volume CFD code, CALC-PMB (Parallel MultiBlock), was developed. The main features of the code are the use of conformal block structured boundary fitted coordinates, a pressure correction scheme (SIMPLEC), Cartesian velocity components as the principal unknowns and a collocated grid arrangement together with Rhie and Chow interpolation. The turbulence is modeled using a low-Reynolds $k - \omega$ turbulence model. The parallel multiblock algorithm employs two ghost cell planes at the block interfaces. The message passing at the interfaces is done using either PVM (Parallel Virtual Machine) or MPI (Message Passing Interface).

Three water turbine runners are used for the investigations, two Kaplan runners and one Francis runner. One of the Kaplan runners was used during the development of the CFD code. This runner could not be used to validate the CFD code but the work on this runner still gave valuable insights on CFD in water turbines. The other Kaplan runner is a model of the runners installed in the Hölleforsen power plant in Indalsälven in Sweden. The computational results of the Hölleforsen wicket gate and runner flow are validated against the thorough experimental investigations from the *Turbine 99* workshops and additional LDV (Laser Doppler Velocimetry) measurements made in the present work. The Francis runner model investigated here was used as a test case at a GAMM workshop in 1989. The present computational results

of the GAMM Francis runner are validated against measurements at both the best efficiency operating condition and four off-design operating conditions. Several important flow features are visualized to make comparisons with experimental observations and to better understand the flow in water turbine runners. The validations against both detailed measurements and experimental observations show that the flow is captured qualitatively correctly.

A method for numerical verification of the computational results has been derived and applied to the computational results of the present work. The method is based on the conservation of a sub-set of the angular momentum equations that is particularly important to swirling flow in water turbines. The method is based on the fact that the discretized angular momentum equations are not necessarily conserved when the discretized linear momentum equations are solved. The method shows that the first-order hybrid discretization scheme cannot be used and that the second-order Van Leer discretization scheme needs improvement to give quantitatively correct results in these kinds of applications.

Keywords: CFD, Numerical, Parallel, Multiblock, Kaplan, Francis, Turbine, Validation, Verification, Visualization

Preface

This thesis starts with a short introduction to the topic of water turbines and a short description of the present work. This is followed by a summary of the attached papers, conference contributions and internal reports that cover most aspects of the work. The thesis continues by giving some results not included in the attached papers and finishes with some conclusions and proposals for future work. Most of the technical details of the methods used in the work can be found in the appendix or in the references.

The thesis is based on the work reported in papers I - VIII:

- I. H. Nilsson and L. Davidson
"A Numerical Comparison of Four Operating Conditions in a Kaplan Water Turbine, Focusing on Tip Clearance Flow"
In Proceedings of *20:th IAHR Symposium, Charlotte, USA*, 2000.
- II. H. Nilsson, S. Dahlström and L. Davidson
"Parallel Multiblock CFD Computations Applied to Industrial Cases"
In Proceedings of *Parallel Computational Fluid Dynamics - Trends and Applications, Trondheim, Norway*, pages 525-532, 2001.
- III. H. Nilsson and L. Davidson
"A Validation of Parallel Multiblock CFD Against the GAMM Francis Water Turbine Runner at Best Efficiency and Off-design Operating Conditions"
Report 01/2, Department of Thermo and Fluid Dynamics, Chalmers University of Technology, Göteborg, Sweden, 2000.
- IV. H. Nilsson, U. Andersson and S. Videhult
"An Experimental Investigation of the Flow in the Spiral Casing and Distributor of the Hölleforsen Kaplan Turbine Model"
Report 01/5, Department of Thermo and Fluid Dynamics, Chalmers University of Technology, Göteborg, Sweden, 2000.

- V. H. Nilsson and L. Davidson
"A Numerical Investigation of the Flow in the Wicket Gate and Runner of the Hölleforsen (Turbine 99) Kaplan Turbine Model"
In Proceedings of *Turbine 99 - II, Älvkarleby, Sweden*, 2001.
- VI. H. Nilsson and L. Davidson
"Validations of Finite Volume CFD Against Detailed Velocity and Pressure Measurements in Water Turbine Runner Flow"
Submitted for journal publication, 2002.
- VII. H. Nilsson and L. Davidson
"Application of a Momentum-Imbalance Method for Investigating Numerical Accuracy in Swirling Flow"
Submitted for journal publication, 2002.
- VIII. H. Nilsson and L. Davidson
"Validations and Investigations of the Computed Flow in the GAMM Francis Runner and the Hölleforsen Kaplan Runner"
Accepted for publication in the Proceedings of *21:st IAHR Symposium, Lausanne, Switzerland*, 2002.

Acknowledgments

In the spring of 1996 I walked into the office of Professor Lars Davidson. I was looking for a method to investigate secondary flow features over sedimentary furrows, the topic of the thesis for my Master of Science in Oceanography. He indeed had a method, and I finished my master thesis with Lars as my co-supervisor. I'm not really sure what happened, but I didn't actually study the secondary flow features over sedimentary furrows in the thesis. Lars had other plans and lead me into work on the implementation of a parallel multiblock CFD code that could be used to compute the flow in complex geometries. Then he offered me the five years of Ph.D. study on the flow in water turbine runners that is presented in this work. And he still wants me to stay! Thank you Lars, I've had a great time so far, so why not! ... But I still wonder what happened with the sedimentary furrows ...

I am grateful to the organizations that financed this work as part of a Swedish water turbine research programme: ELFORSK (Swedish Electrical Utilities Research and Development Company), the Swedish National Energy Administration and GE Energy (Sweden) AB. I would like to mention some of the people in the programme with whom I have enjoyed particularly close collaboration: Cristian Andersson, who is exemplary at coordinating the programme; Bengt Nauclér, who has been my industrial mentor and has supplied me with invaluable information; Rolf Karlsson, Urban Andersson and Sebastian Videhult with whom I have had fruitful discussions and good collaboration in experimental fluid dynamics; the rest of the Ph.D. students in the water turbine programme – I think we've had a good time. The people involved in the reference group are acknowledged for their feedback.

I would like to thank the following organizations for our collaboration throughout this work: LMH-IMHEF-EPFL, and particularly Prof. Francois Avellan, for letting me work at his Department for three months; Vattenfall Utveckling AB, and its staff, for their contribution of equipment and knowledge; CERCA, and particularly Dr. Chantal

Pic in Montreal, Canada, for virtual reality visualization; Chalmers Medialab for virtual reality visualization; UNICC for computational resources and MDC for computer support.

I would like to thank the following people who have contributed to this work in one way or another: Simon Dahlström, who made many of the speed-up tests in Paper II; Anders Ålund, who helped me use PVM during the early stages of the implementation of the code; Janet Vesterlund, who is one of the few people that have read every word I have written – thank you for proofreading my papers! Sandra, Ulla and Monika – you’re doing a great job! The rest of the people at the Department – I don’t need to remind you of the nice atmosphere we have.

I would like to end this acknowledgement by mentioning some people that have had a great influence on my life: The surfers of Falkenberg – you are the true experts in practical fluid dynamics. Surfing is actually the reason that I ended up here and I will always be a surfer. Hang loose! My parents, Eva and Bengt, who have done (and still do) everything for me, my brother and our families. I hope that I will be as good a parent. My brother and his family, Anders, Camilla, Felicia and Hanna – you mean a lot to me.

My wife Maria and our daughter Emmy – the meaning of life – I love you both!

If you feel that you have been left out I must have forgot to include your name above. Please write your name here

.....
and you are gratefully acknowledged.

Contents

Abstract	iii
Preface	v
Acknowledgments	vii
1 Introduction	1
1.1 Introduction to water turbines	2
1.1.1 Water turbine runners	3
1.1.2 The reaction turbine working process	7
1.1.3 Flow features in water turbine runners	8
1.2 A short description of the work	11
1.2.1 The first Kaplan runner	14
1.2.2 The GAMM Francis runner	15
1.2.3 The Hölleforsen Kaplan runner	16
2 Summary of the papers	21
2.1 Paper I	21
2.2 Paper II	22
2.3 Paper III	22
2.4 Paper IV	23
2.5 Paper V	24
2.6 Paper VI	26
2.7 Paper VII	27
2.8 Paper VIII	28
3 Further investigations of the Hölleforsen runner flow	31
3.1 The measurements	31
3.2 The computations	35
3.3 How to compare the computational results with the measurements	39

3.4	Comparisons at section Ia	43
3.5	Comments to the phase resolved comparisons	49
4	Unsteady computations of the Hölleforsen runner flow	55
4.1	The unsteady inlet boundary condition	56
4.2	Preliminary results	57
4.3	Discussion	61
5	Conclusion	63
	Bibliography	65
A	Governing equations	71
A.1	Continuity and momentum equations	71
A.2	Turbulence modelling	72
A.3	Summary of the solved equations	75
B	The code	77
B.1	The finite volume method	77
B.2	Spatial discretization schemes	81
B.2.1	The central scheme	81
B.2.2	The first-order upwind scheme	81
B.2.3	The hybrid scheme	82
B.2.4	The Van Leer Scheme	82
B.3	Pressure-velocity coupling	83
B.3.1	The SIMPLEC method	83
B.3.2	Rhie & Chow interpolation	85
B.4	Boundary conditions	87
B.4.1	Walls	87
B.4.2	Inlet/outlet conditions	88
B.4.3	Periodic boundaries	89
B.5	Solving the discretized equations	89
B.6	Convergence criteria	90
B.7	The parallel multiblock implementation	90
B.7.1	Numerical procedure	92
C	PAPERS	95

Chapter 1

Introduction

Sweden has used water power since the 19th century and about 50% of the electrical power in Sweden is currently produced by water power. The main efforts in research and education on and the design of water turbines in Sweden took place between 1930 and 1960. Most of the people working with water turbines at that time are no longer active in the business, and the number of manufacturers has fallen substantially. The present work is part of a programme financed by a collaboration between the Swedish power industry via ELFORSK (Swedish Electrical Utilities Research and Development Company), the Swedish National Energy Administration and GE Energy (Sweden) AB. The purpose of the programme is to raise Swedish water power competence in order to meet the growing demand for water power in Sweden together with the demands on environmental care and efficiency.

New water turbine runners are traditionally tested using expensive and time-consuming model tests. A Francis model runner costs about SEK 250,000 and takes a minimum of three weeks to manufacture. The Kaplan model runner blades cost about SEK 100,000 and take about five weeks to manufacture. The model testing is an iterative procedure where the impact of modifications to the model runner is analysed on the basis of the measurements and experience. The results obtained in the model testing are then scaled up to the actual size turbine using empirically determined relations. It is very important to capture the final turbine efficiency and the power output at the model testing stage. When the final turbine does not meet the specifications the fines may easily be as large as the profits. The present work focuses on how to use CFD (Computational Fluid Dynamics) to accurately predict the turbulent flow in water turbine runners. Accurate CFD can be used as a complement to model testing to speed up the design procedure and to

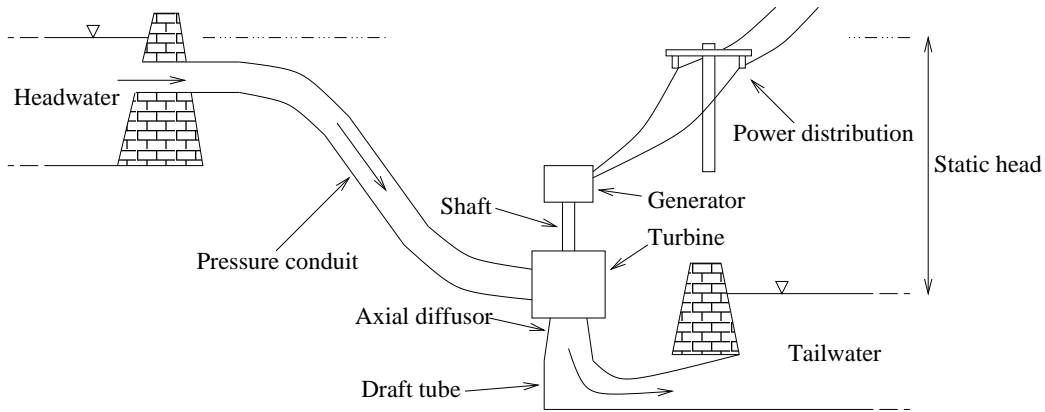


Figure 1.1: Schematic description of a power plant and definitions of some important terms.

reduce the manufacturing cost. Investigations of the computational results can also be used to further understand the details of the flow in water turbine runners.

The following sections introduce the area of water turbines, report on the numerical investigation approach used in this work and give a description of the cases studied.

1.1 Introduction to water turbines

Water turbines are designed to extract energy from the water that flows through it. Figure 1.1 shows a schematic description of a power plant and defines some important terms. The water used in water turbines possesses energy in the form of potential energy. The water power that is available for electrical power generation is given by $P_w = \rho Q g H$ [W], where ρ [kg/m^3] is the density of the water, Q [m^3/s] is the water volume flow, g [m/s^2] is the gravity acceleration and H [m] is the difference in elevation (static head) between the inlet (headwater) and outlet (tailwater) of the power plant. P_w was derived assuming that the difference in kinetic energy between the inlet and outlet of the power plant is small, and that there are no hydraulic losses. The actual electrical power that is generated from the power plant is $P_e = \eta_t \rho Q g H$ [W], where η_t [-] is the total efficiency of the power plant. The total losses include hydraulic losses in the conduits supplying water from the headwater, in the turbine, and in the conduits through which water is discharged

from the turbine into the tailwater. The total losses also include non-hydraulic losses such as power transmission through the turbine shaft and electricity generation in the generator.

To further investigate the turbine working process we need to know more about the working parts of the water turbine, which is discussed in the next sections.

1.1.1 Water turbine runners

A water turbine consists of three main parts: the runner, which is attached to a rotating shaft, devices that supply water to the runner, and devices through which water is discharged from the runner. The different kinds of water turbine runners that are available can be grouped according to the flow in the runner, which may be axial, mixed-flow, radial-axial or tangential. Axial, mixed-flow and radial-axial runners are usually reaction runners, while tangential runners are impulse runners. Only axial and radial-axial runners are studied in this work and they are described in the following sections. Mixed-flow runners are similar to axial runners but the runner blades are mounted at an angle to the axis of rotation. Mixed-flow runners are used at heads between $40m$ and $100m$. Pelton turbines have impulse runners, where all the static head is used to form high-speed jets ($\sim 100m/s$) in nozzles before the runner. Most of the kinetic energy of the water jets is extracted by the buckets of the Pelton runner, and the water falls through air to the floor and exits the turbine. Pelton turbines are used at heads over $400m$.

Axial flow turbine runners

The water flow through axial flow turbine runners is axial all the way through the runner, which gives them the name axial flow turbines. Axial flow turbines are usually used in heads ranging from $1m$ to $70m$. Axial flow turbines may have adjustable runner blades or fixed runner blades. A runner with adjustable runner blades is called a Kaplan runner and a runner with fixed runner blades a propeller runner. The advantage of using adjustable runner blades is that the efficiency is higher over a wider operating range, which allows the available water power, P_w , to change without losing a great deal in efficiency. Figure 1.2 is an illustration of a Kaplan turbine. The water flow is from the pressure conduit into the inlet of the spiral casing. The spiral casing usually consists of a trapezoidal cross-section made of concrete. Spiral casings

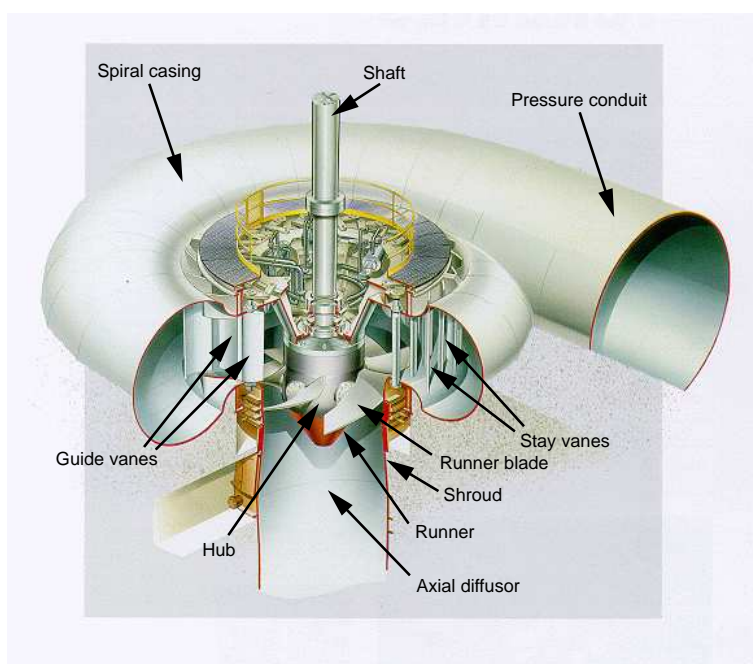


Figure 1.2: A Kaplan water turbine. Parts of the casing are removed in the illustration in order to show the interior parts. Picture courtesy of GE Energy (Sweden) AB.

with round cross-sections of steel (as in figure 1.2) are constructed only at relatively high heads. Inside the spiral casing the water flow is more or less uniformly distributed to the stay vanes and guide vanes. The stay vanes, which strengthen the structure, are streamlined to minimize the hydraulic losses. The wicket gate (the guide vane cascade) consists of 20 to 32 guide vanes that are adjustable and control the volume flow and influence the runner inlet swirl. The number of runner blades may vary from four to eight. In operation, the Kaplan runner blade angle is correlated with the guide vane angle to obtain maximum efficiency. The hub and shroud shapes are spherical at the runner blades to minimize the clearances that are unavoidable with adjustable blades. The smaller the gap, the smaller the leakage and the higher the turbine efficiency. After the runner the water flows axially into a straight diffuser, which recovers some of the remaining kinetic energy. Excluded in this picture is the draft tube (see figure 1.1), which is a diffuser that recovers more of the remaining kinetic energy and leads the water to the tailwater. The draft tubes of high-capacity turbines are always made of concrete.

The Kaplan turbine runner was invented in 1913 by Victor Kaplan from Czechoslovakia. A patent was granted in 1917 and the first Kaplan turbine was commissioned in 1919 in the Velma River. This first Kaplan runner had a diameter of 0.6m and a head of 3m . The first large dimension Kaplan turbine in the world was ordered in 1922 from the company that is presently called GE Energy (Sweden) AB. This resulted in the unit at Lilla Edet in Sweden, which has a runner diameter of 5.8m , an output of 8.2MW and a head of 6.5m .

Radial-axial flow turbine runners

The water flow through radial-axial flow turbine runners is both radial and axial, hence the name radial-axial flow turbines. Francis turbines are radial-axial flow turbines. Francis turbines are usually used in heads ranging from 40m to 700m . Figure 1.3 is an illustration of a Francis turbine. The water flow is from the pressure conduit into the inlet of the spiral casing. The spiral casing consists of a round cross-section made of steel to improve the conditions under which the walls take up the water pressure load of the high head. Inside the spiral casing the water flow is more or less uniformly distributed to the stay vanes and guide vanes. The stay vanes, which give the structure strength, are streamlined to minimize the hydraulic losses. The wicket gate consists of 20 to 24 guide vanes that are adjustable and control the volume flow

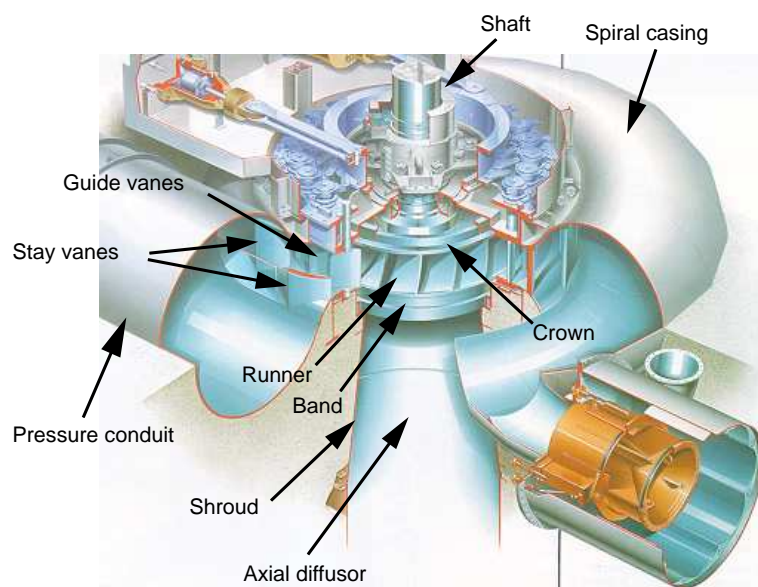


Figure 1.3: A Francis water turbine. Parts of the casing are removed in the illustration in order to show the interior parts. Picture courtesy of GE Energy (Sweden) AB.

and influence the runner inlet swirl. Francis turbine runners consist of 12 to 17 blades that are fixed rigidly in the crown and the band to attain the required strength and rigidity. There are thus no tip clearances in Francis runners. After the runner the water flows axially into a straight diffuser, which recovers some of the remaining kinetic energy. Excluded in this picture is the draft tube (see figure 1.1), which is a diffuser that recovers more of the remaining kinetic energy and leads the water to the tailwater.

1.1.2 The reaction turbine working process

All reaction turbines work in a very similar way. The differences lie in the operating range. In reaction turbines the water volume flow, Q [m^3/s], through the turbine is determined by the opening of the wicket gate (the guide vane cascade). Some of the static energy of the water is converted to the kinetic energy of a swirling flow component after the guide vane passage. The swirling flow enters the runner, where the water power is extracted. The power that is converted to the useful power of the rotating shaft can be estimated by the change in angular momentum about the axis of rotation as the water flows past the runner. The general Euler equation for turbomachinery relating the input shaft power to the change in angular momentum for the flow in a thin stationary axisymmetric stream tube (see Figure 1.4) can be written [11]

$$-\Delta P_{shaft} = \Delta \dot{m} \Omega (r_2 U_{\theta 2} - r_1 U_{\theta 1}) \quad (1.1)$$

where $\Delta P_{shaft} = \Delta T \Omega$ [W], ΔT [Nm] is the runner torque of the stream tube, $\Delta \dot{m}$ [kg/s] is the mass flow through the stream tube, Ω [s^{-1}] is the runner rotation, r [m] is the mean radius and U_{θ} [m/s] is the velocity in the tangential direction in an inertial coordinate system. Index 1 denotes *before* the runner and index 2 denotes *after* the runner, which should be located far from the runner blades so that the properties can be assumed to be axisymmetric and uniform over the width of the thin stream tube. A non-swirling runner outlet flow ($U_{\theta 2} = 0$) gives the best condition. Equation 1.1 is valid for a thin stationary axisymmetric stream tube where there is no mass, momentum or energy transfer through the stream tube surfaces except at 1 and 2. The input shaft power of the general Euler equation in a stationary coordinate system acts as tangential 'body forces' that change the angular momentum in the runner blade region. The sum of the power from all stream tubes

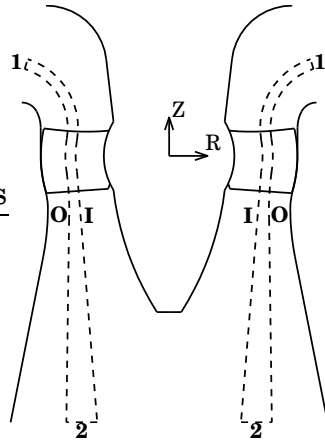


Figure 1.4: A thin axisymmetric 'stream tube' / control volume (dashed lines) going through the runner region. The control volume inlet and outlet are marked 1 and 2, respectively. The inner (I) and outer (O) control surfaces are Euler 'stream surfaces', where there is no mass, momentum or energy transfer.

that cross the runner blades can be related to the available water power as

$$P_{shaft} = \eta_h \rho Q g H$$

where $\eta_h [-]$ is the hydraulic efficiency.

As the water flows through the wicket gate and the runner the static pressure is reduced. The static pressure may actually be reduced below atmospheric pressure and at some operating conditions may be locally reduced to a level where the water cavitates. As the water flows through the diffusing draft tube into the tailwater the kinetic energy is reduced and some of the static pressure is recovered. Studying the flow in the draft tube however is beyond the scope of this work.

1.1.3 Flow features in water turbine runners

Water turbine runners have many undesirable flow features. Some of these are friction losses, guide vane wake interaction, tip clearance flow, hub clearance flow, cavitation and the secondary flow produced by these, not to mention the remaining swirl caused by inefficient runner blade profiles and off-design operating conditions.

First of all, the Reynolds number in water turbine runner models is approximately $Re = \Omega R^2 / \nu \approx 4 \cdot 10^6 [-]$, where $\Omega [s^{-1}]$ is the runner

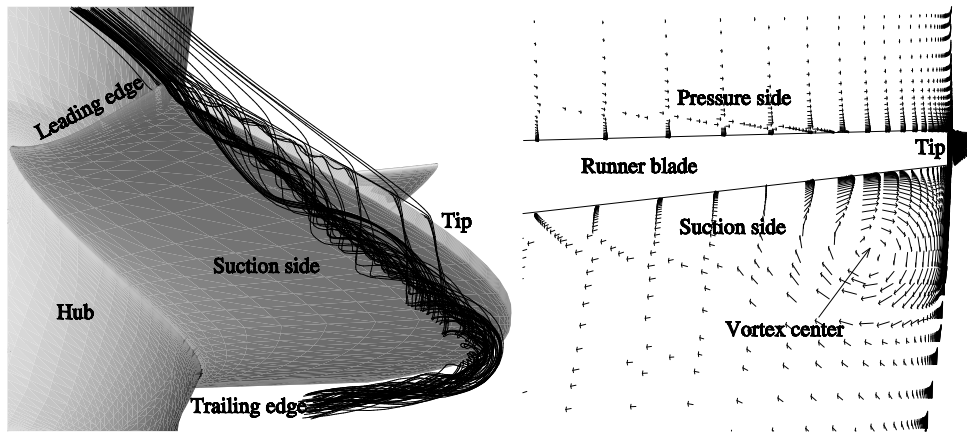


Figure 1.5: Streamlines and vectors visualizing a predicted Kaplan tip vortex at an off-design operating condition.

rotation, R [m] is the runner radius and $\nu = 10^{-6} m^2/s$ is the kinematic viscosity of water at $20^\circ C$. High Reynolds number flows like this have very thin boundary layers that should be resolved in an accurate numerical prediction. The great differences in geometrical and flow scales make grid generation, numerical convergence and turbulence modelling a challenging task.

The main purpose of this work is to predict the flow in the tip clearance between the Kaplan runner blade tips and the shroud. Kaplan runner tip clearances have a width of about 0.1% of the runner radius, and the flow through the tip clearances reduces the efficiency of the turbine by about 0.5%. The reduction of the efficiency due to the tip clearance flow may seem small but water turbine efficiencies are very high (about 95%) and the improvements that can be made are in the range of 0.1% in efficiency. The tip clearance flow is driven by the static pressure difference between the pressure and suction sides of the blade. The tip clearance flow produces a jet at the exit to the suction side, where it interacts with the shroud boundary layer and forms a vortical structure along the tip on the suction side of the runner blade. Figure 1.5 gives an example of a Kaplan tip vortex at an off-design operating condition that was predicted in this work.

The static pressure is reduced at the center of vortices, which may cause the water to cavitate (figure 1.6). Cavitation bubbles formed in the tip vortex follow the flow and may implode close to the tip at the center of the suction side, causing severe damage to the runner blade. The loss of efficiency caused by the tip clearance flow and damage to



Figure 1.6: Hub and tip clearance cavitation. The picture shows the suction side of a Kaplan runner blade. The leading edge is at the upper left and the trailing edge is at the lower right. The hub is to the left. The cloudy structure close to the hub and the streaky structure close to the blade tip are cavitation bubbles that have developed in low static pressure regions. Picture courtesy of M.Grekula and G.Bark, Department of Naval Architecture and Ocean Engineering, Division of Hydromechanics, Chalmers University of Technology.

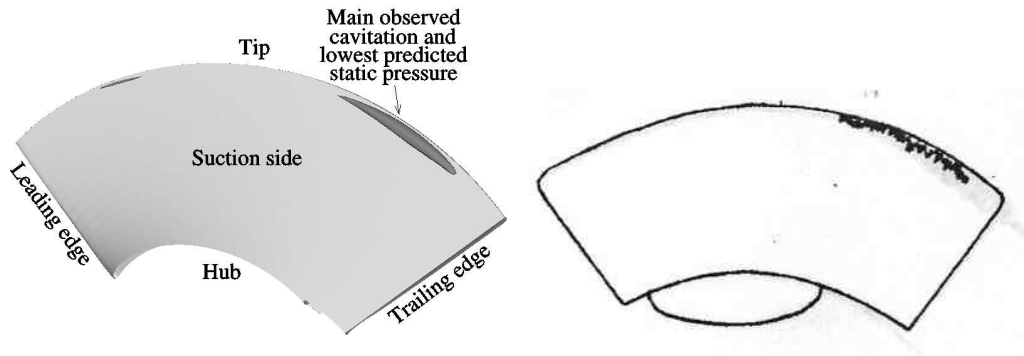


Figure 1.7: Comparison between the lowest predicted static pressure region (dark grey iso-surface) and observed cavitation behavior at the best efficiency operating condition of the Hölleforsen Kaplan runner. The cavitation behavior was observed in 1955 at a model test of a very similar runner at roughly the same operating conditions as the computations (Picture courtesy of GE Energy (Sweden) AB).

the runner blades are very expensive. The present work studies non-cavitating (single phase) flow, which means that cavitation is not included in the computations. Some indications on the cavitation behavior of the flow in the runner may however be visualized as regions of low static pressure. Figure 1.7 compares predicted and experimentally observed low static pressure regions and cavitation behavior of the Hölleforsen Kaplan runner. The discussion of cavitation highlights the necessity of capturing the details of the flow in water turbines.

1.2 A short description of the work

Water turbines have been investigated numerically for decades. There are 1D, 2D, quasi-3D and 3D numerical methods that approximate the flow in water turbines with increasing levels of accuracy and detail. The Euler method is an example of a 3D numerical method that neglects the effects of viscosity and turbulence. The present work studies a 3D numerical method that includes the effects of viscosity and models the effects of turbulence. During the most recent decades the computational methods for turbomachinery have been undergoing a transition from inviscid flow to viscous flow. Some of the assumptions made in the inviscid methods are thus being rejected in order to make more accurate predictions of the flow. Numerous additional flow features are

added in viscous flow. These flow features are neglected or modeled in the less accurate methods. Since most of the experience with numerical methods in water turbines originates from the less accurate methods, new experience with viscous (and turbulent) numerical methods must be gathered. The present work contributes to the total experience of viscous numerical methods in water turbine computations.

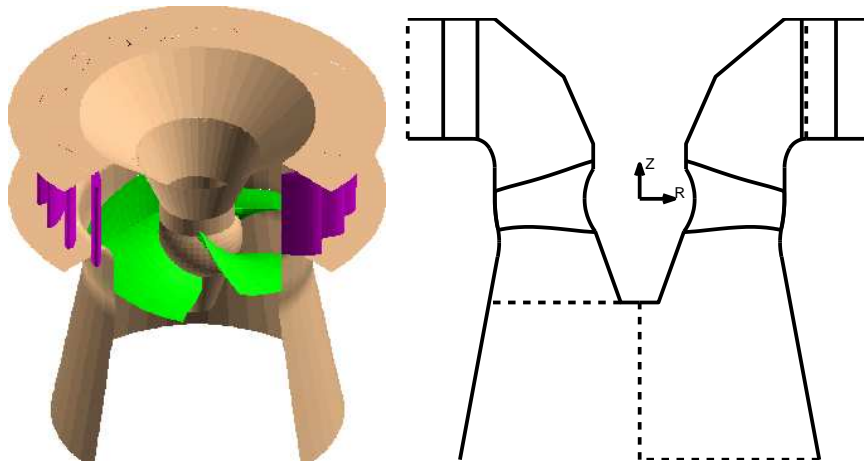
The basis of the method used in the present work is that the viscous fluid flow equations that include a model for the turbulence (see Appendix A.2) are discretized in space (and time, when making unsteady computations). The *finite volume* method (see Appendix B.1) used in this work subdivides the flow region into a large number of control volumes and computes the flow properties at the center of all the control volumes. These control volumes can have different shapes, but in this work are hexahedral (six faces and arbitrarily placed vertices). A number of control volumes can be connected face-to-face to form a 3D region of $l \times m \times n$ control volumes, called a *structured block*. If l , m and n are sufficiently large numbers this block can be used to describe the geometry of a fairly complicated flow region. However, if the flow region is more than fairly complicated a *single block* representation requires the control volumes to be extremely skew, which introduces numerical errors and convergence problems when solving the discretized equations. A solution to this is to connect a number of structured blocks subface-to-subface, which results in an *unstructured multiblock topology* of structured blocks (see Appendix B.7). Using this approach all kinds of flow geometries may be described with sufficiently orthogonal control volumes. Sharp gradients of the flow may be resolved by adjusting the aspect ratio of neighboring control volumes. This approach can thus be used to resolve both the flow geometry and the flow features. The first part of the present work was to implement such a multiblock finite volume solver (see Appendix B) and an interface to the ICEM CFD commercial CAD and grid generation software that can generate general multiblock topologies.

When all the important aspects of both the geometry and the flow are resolved the number of control volumes in the computational domain is usually very large. This means that the requirements on the computational resources (with respect to both CPU speed and memory size) are also very large and it requires a very long time to obtain a solution to the discretized problem. The computational speed can be increased significantly however by letting several CPUs simultaneously compute different parts of the problem. If this is done correctly the RAM memory and cache memory requirements are also distributed amongst

the CPUs. In the implementation in the present work the computational blocks are assigned to different PVM (Parallel Virtual Machine) or MPI (Message Passing Interface) processes that are distributed on separate CPUs (see Paper II and Appendix B.7). The coupling between the blocks is taken care of using a high level multiblock library in the finite volume code and the built-in functions of PVM or MPI. The calls for parallel multiblock routines in the code are completely independent of the message passing system used. The user of the code decides which message passing system to use at compile time and the code may be run on everything from heterogeneous networks of workstations to Linux clusters and distributed and shared memory super computers.

The main goal of the present work is to correctly predict the flow in the clearance between the Kaplan runner blades and the shroud. A necessary condition for accurate predictions of the tip clearance flow is to predict the rest of the flow correctly. The computational technique must thus be validated against detailed measurements. It is difficult, however, to find detailed measurements of the flow in water turbines since manufacturers withhold this information. Most often, no detailed measurements are made at all, since it is the overall quantities, such as efficiency, that are important in marketing the product. This work validates the computational technique against detailed measurements of both a Kaplan runner and a Francis runner. The measurements are made both in the present work and by others. The Francis runner has no tip clearances and a geometry that is very different from a Kaplan runner. The two types of turbines are however very similar with respect to the overall flow features. It is thus both relevant and important to validate the computational technique against both types of water turbines. The code has also been validated in parallel Ph.D. projects in academic test cases and in other industrial applications such as LES (Large Eddy Simulations) of the flow around vehicles [9] and airfoils [4], and heat transfer in gas turbines [20].

The computational results have also been verified using a numerical verification method that was developed in the present work (Paper VII). The method is based on the conservation of a sub-set of the angular momentum equations that is particularly important to swirling flow in water turbines. The method is based on the fact that the discretized angular momentum equations are not necessarily conserved when the discretized linear momentum equations are solved. The method shows that the first-order hybrid discretization scheme cannot be used and that the second-order Van Leer discretization scheme needs improvement to give quantitatively correct results for these kinds of



(a) The geometry.

(b) Schematic meridional description.

Figure 1.8: The first Kaplan runner geometry, meridional contour (solid lines) and the domains computed (dashed lines). The left domain is the guide vane domain, with a radial inlet outside the guide vanes and an axial outlet below the runner. The right domain is the runner domain, with a radial inlet at the trailing edge of the guide vanes and an axial outlet at the lower part of the figure. Note that the runner blades are not included in the guide vane computations and the guide vanes are not included in the runner computations.

applications.

The following sections describe the three different water turbine runners (two Kaplan runners and one Francis runner) investigated in the present work.

1.2.1 The first Kaplan runner

The first Kaplan runner geometry used in the present work was obtained from Kvaerner Turbin AB in Kristinehamn, Sweden. Kvaerner Turbin AB was later taken over by GE Hydro and the Swedish lab was re-named GE Energy (Sweden) AB. Figure 1.8 shows the geometry of the first Kaplan runner, which has four runner blades and 24 guide vanes. The runner diameter is $0.5m$ and the tip clearance $0.25mm$. The present work studies four operating conditions with decreasing runner speed, increasing blade loading and increasing tip clearance flow. The

runner blade angle is the same for all the operating conditions so that it was possible to use the same grid in all the cases. The chosen runner blade angle gave a constant tip clearance width from the runner blade leading to trailing edges.

This runner was used during the development of the code. It was found that the runner blade angle made it very difficult to generate a good grid that resolved both the boundary layers and the tip clearance with the ICEM CFD grid generation features available at that time. It was also found that the constant and very small width of the tip clearance gave a very small tip vortex that was difficult to observe. A major drawback of this runner is that there are no detailed measurements of the flow. The only information available on this runner is the geometry, the guide vane angle, the runner blade angle, the volume flow, the head, the efficiency, the torque and some general observations made by the turbine manufacturer. It could thus not be used to validate the details of the computational results.

The first computations for this runner were presented in a Licentiate thesis [14] and at the *Hydropower Into the Next Century* conference [16]. These computations assumed an axisymmetric fully developed turbulent 1/7 profile at the trailing edges of the guide vanes. The flow angle was assumed in this case to be aligned with the guide vanes. The flow equations were discretized with the first-order hybrid scheme, which was stable enough to give a solution. Subsequent computations have used the circumferentially averaged results of separate guide vane computations as inlet boundary conditions and the second-order Van Leer discretization scheme (see Paper I). All computations assumed the flow to be steady and periodic over a single blade. No validations against measurements could be made but the work on this runner highlighted the importance of using a higher-order discretization scheme when computing the flow in water turbine runners (see Paper VII).

1.2.2 The GAMM Francis runner

The GAMM (Gesellschaft für Angewandte Mathematik und Mechanik) Francis runner work was initiated out of a need to validate the CALC-PMB CFD code for hydraulic turbine applications. The code had previously been validated against academic flow cases but not for applications as geometrically complicated as hydraulic turbines. The GAMM Francis runner model was designed at IMHEF (Institut de Machines Hydrauliques et de Mécanique des Fluides) at EPFL (École Polytech-

nique Fédérale de Lausanne) for experimental research in the LMH (Laboratoire de Machines Hydrauliques) hydraulic laboratory. The model was used as a test case at the 1989 GAMM workshop, where all the geometrical information, including stay vanes, guide vanes, runner and draft tube, and the best efficiency measurements were available. The GAMM runner is also used as a test case in the annual ERCOFTAC (European Research Community On Flow Turbulence And Combustion) Seminar and Workshop on Turbomachinery Flow Predictions. Of course, several off-design operating condition measurements have been made at IMHEF for internal use. Some of these measurements, namely the best efficiency operating condition and four off-design operating conditions, are used in this work.

Figure 1.9 describes the GAMM runner geometry, the measurement sections and the computational domain. The GAMM runner has 13 blades with a runner diameter of $0.4m$. The present work computes the steady periodic flow of a single runner blade. The computational domain starts at the guide vanes, where inlet boundary conditions derived from an extrapolation of the measurements before the runner blades are applied. The guide vanes are not included in the present work and the computational domain ends at the end of the axi-symmetric diffuser, before the draft tube bend.

The present work compares the computational results of the GAMM runner with measurements of the circumferentially averaged velocity and static pressure distributions, the runner blade static pressure distributions, the torque, the specific energy and the efficiency (see Paper III). The comparisons show that the code predicts the flow in the GAMM runner well and that the parallel multiblock CALC-PMB CFD code can be relied upon to predict the turbulent flow in hydraulic machinery.

1.2.3 The Hölleforsen Kaplan runner

The Hölleforsen model is a model of the Kaplan turbines of the Hölleforsen power plant installed in Indalsälven in Sweden in 1949. The head of the power plant is $27m$ and consists of three Kaplan turbines with a runner diameter of $5.5m$, a maximum power of $50MW$ and a flow capacity of $230m^3/s$ per turbine. The Hölleforsen model runner has a diameter of $0.5m$. The model has five runner blades and 24 guide vanes. The tip clearance between the model runner blades and the shroud is $0.4mm$. Figure 1.10 shows the Hölleforsen model wicket gate and runner geometry, the measurement sections and the computatio-

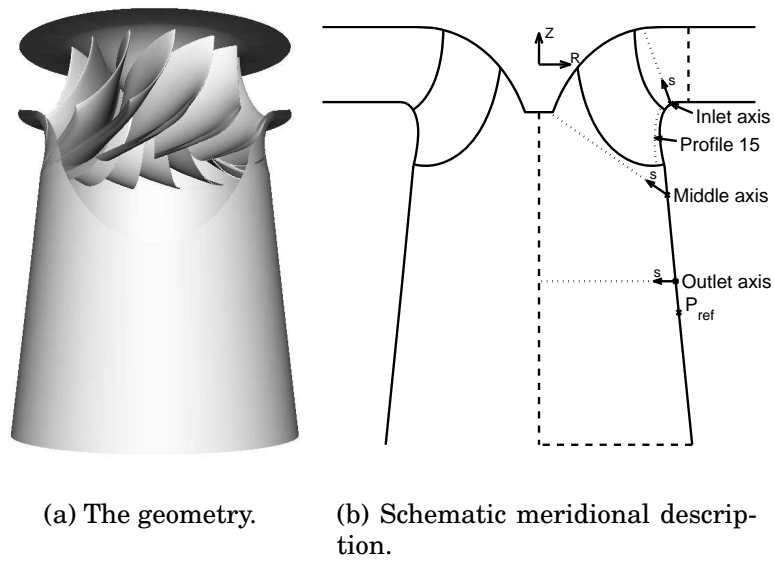


Figure 1.9: The GAMM Francis runner geometry, meridional contour (solid lines) and the domain computed (dashed lines). The domain has a radial inlet at the top and an axial outlet at the lower part of the figure. The dotted lines are sections in which the results are compared with measurements. Note that the inlet boundary conditions are extrapolated from the measured inlet axis to the inlet of the computational domain.

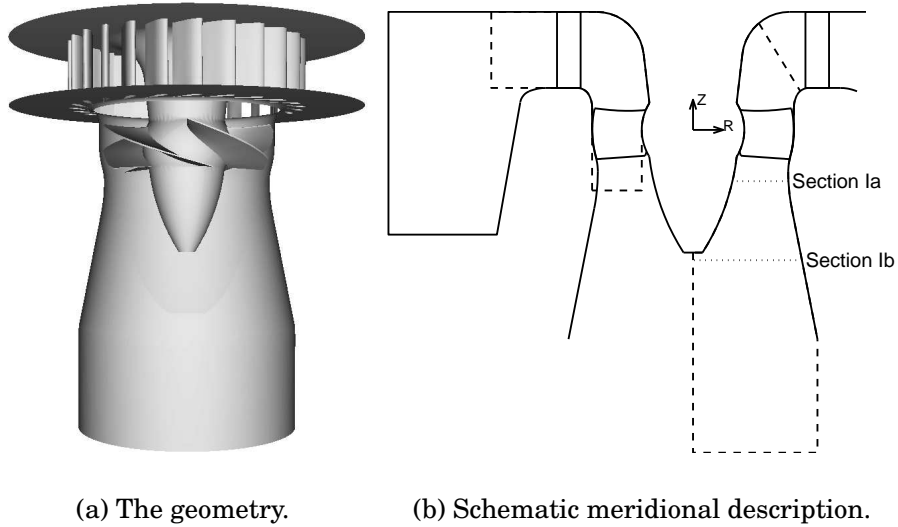


Figure 1.10: The Hölleforsen wicket gate and runner geometry, meridional contour (solid lines) and the domains computed (dashed lines). The left domain is the guide vane domain, with a radial inlet in the spiral casing region and an axial outlet in the runner region. The right domain is the runner domain, with a tilted inlet between the guide vanes and the runner blades and an axial outlet at the lower part of the figure. The dotted lines are sections in which the results are compared with measurements. Note that the runner blades are not included in the guide vane computations and the guide vanes are not included in the runner computations.

nal domains.

The Hölleforsen model draft tube was thoroughly investigated at the 1999 *Turbine 99* and 2001 *Turbine 99 - II* workshops on draft tube flow. The draft tube geometry and detailed velocity and pressure measurements were available at the workshops. Measurements were made at several sections, starting with a section just after the runner and ending with a section at the end of the draft tube. The measurements made after the runner were used as inlet boundary conditions for the *Turbine 99* draft tube computations. Some assumptions were made on the quantities that could not be measured at the draft tube inlet. The flow in the Hölleforsen Kaplan runner model that supplied the draft tube inlet flow conditions was not included in the investigations, however, since the runner geometry is not publically available. The runner geometry was made available for this work since the GE Energy

(Sweden) AB Hölleforsen runner manufacturer was one of the collaborative partners in the work. Most of the measurements and the computations were made at a head of $H = 4.5m$, a runner speed of $N = 595rpm$ and a volume flow of $Q = 0.522m^3/s$. This operating condition is close to the best efficiency operating point at 60% load and was referred to as test case T (top point of the propeller curve) at the *Turbine 99* workshop.

The present work numerically studies the flow in the Hölleforsen model wicket gate and runner and compares the computational results to the *Turbine 99* measurements (see Paper V). The computations are also compared with LDV measurements of the wicket gate flow made as part of this work (see Paper IV). The computations capture most of the measured and observed flow features in the vicinity of the runner. The computational results thus supplement the experimental results and add to the knowledge of the flow in the Hölleforsen Kaplan model.

Chapter 2

Summary of the papers

This chapter summarizes the attached papers, conference contributions and internal reports, which cover most of the aspects of the present work. The papers are numbered in chronological order. Further work not included in the attached papers is reported in Chapters 3 and 4.

2.1 Paper I

This paper, “*A Numerical Comparison of Four Operating Conditions in a Kaplan Water Turbine, Focusing on Tip Clearance Flow*”, was presented at the *20th IAHR Symposium* in Charlotte, North Carolina, USA, in 2000. The work presents computational results of the first Kaplan runner (see Section 1.2.1) using the second-order Van Leer discretization scheme and inlet boundary conditions from separate guide vane computations. The computational results of the steady periodic flow at four different operating conditions are compared and the general Euler equation for turbomachinery [11] is used to investigate the computational results.

It is shown that the runner blade loading and the tip clearance flow increase as the runner speed decreases. This is in accordance with observations made by the turbine manufacturer. Some flow features are visualized to allow a better understanding of the flow in water turbine runners. Experimentally observed cavitation behavior of the runner flow is used to explain and validate the computational results.

2.2 Paper II

This paper “*Parallel Multiblock CFD Computations Applied to Industrial Cases*”, was presented at the *Parallel Computational Fluid Dynamics - Trends and Applications* conference in Trondheim, Norway, in 2000. The work discusses some parallelization aspects of the CALC-PMB CFD code that was developed in the present work. The parallel efficiency and the load balance issues are discussed for computations of both water turbine runners, a high-lift airfoil [4] and an academic test case. The tests were made on two different super computer architectures.

It is shown that the parallel efficiency is excellent, with super scalar speed-up for load balanced applications using the best configuration of computer architecture and message passing interface. For water turbine runner computations, however, it is shown that it is difficult to obtain load balanced computations with the present approach, and the parallel efficiency may drop rapidly. It is discussed that the load balance problem can be handled by a re-distribution of the multiblock topology or by time sharing of small blocks on shared CPUs. A comparison of load balanced airfoil computations using two different computer architectures and different message passing interfaces shows that a poor combination of computer architecture and message passing interface may drastically reduce the parallel efficiency. In contrast, with a good combination of computer architecture and message passing interface, it is shown that the parallel approach is super scalar up to 32 processors for large load balanced industrial CFD problems.

2.3 Paper III

This paper, “*A Validation of Parallel Multiblock CFD Against the GAMM Francis Water Turbine Runner at Best Efficiency and Off-design Operating Conditions*”, was written during collaboration with LMH-IMHEF-EPFL in Lausanne, Switzerland, in the autumn of 1999. It was published as an internal report at the Department of Thermo and Fluid Dynamics at Chalmers University of Technology in 2001. Selected parts of this work are also included in other papers.

A thorough description is given of a validation of the CALC-PMB CFD code against the detailed measurements of the GAMM Francis runner (see Section 1.2.2) at best efficiency and off-design operating conditions. The work describes in detail the problems that were en-

countered in making the validation, such as discrepancies in the geometrical information and problems with the experimental data.

The paper compares the computational results of the GAMM runner with measurements of the circumferentially averaged velocity and static pressure distributions, the runner blade static pressure distributions, the torque, the specific energy and the efficiency. The comparisons show that the code predicts the flow in the GAMM runner well. This is particularly true at the best efficiency operating condition. At off-design operating conditions both the measurement technique and the computational technique are inadequate at the measured outlet axis below the runner. This region is characterized by a strong flow unsteadiness, recirculation and non-periodicity. For the comparisons away from this region the computational results and the measurements agree well. Some predicted flow features are visualized to highlight results that correspond to experimental observations, such as recirculation and cavitation.

Experience gained in the computations shows that almost all the convergence problems in all computations have their origin in the flow beneath the hub. It is found that the tangential velocity converges extremely slowly close to the axis of rotation in this region. A proposal for further study of the unsteady non-periodic flow in the diffuser after the runner is made.

The paper concludes that the parallel multiblock CALC-PMB CFD code can be relied upon to predict the turbulent flow in hydraulic machinery.

2.4 Paper IV

This paper “*An Experimental Investigation of the Flow in the Spiral Casing and Distributor of the Hölleforsen Kaplan Turbine Model*”, was written during collaboration with two industrial Ph.D. students at Vattenfall Utveckling AB and GE Energy (Sweden) AB. The work was carried out at the experimental facilities of Vattenfall Utveckling AB in Älvkarleby, Sweden. It was published as an internal report at the Department of Thermo and Fluid Dynamics at Chalmers University of Technology in 2001.

The paper presents LDV (Laser Doppler Velocimetry) measurements of the flow in the spiral casing and distributor of the Hölleforsen Kaplan turbine model (see Section 1.2.3). The measurements are an extension of the measurements for the *Turbine 99* and *Turbine 99 - II*

workshops on draft tube flow, where detailed LDV and pressure measurements were made after the runner. The goal of the present work was to increase knowledge of the flow before the runner and to validate computations of the flow in the spiral casing and distributor.

The measurement sampling rates and times and the spatial resolution were sufficient to get a detailed picture of the mean flow and RMS (Root Mean Square) values in three measurement planes. The measurement planes covered much of the spiral casing and distributor ducts and extended into the trailing edges of the guide vanes. A runner phase signal that correlates the measurement samples with the runner orientation was used to study the influence of the runner blade passages. No such effect could be observed, however, since it was much smaller than the effect from the turbulent fluctuations. This result shows that the velocity distribution in the guide vane passage is not significantly influenced by the runner blade passage and that the flow in the guide vane passage can be computed separately.

The measurements revealed a local increase in the magnitude of the radial velocity in the boundary layer at the top of the spiral casing. This behavior has been observed before, both experimentally and numerically, in the flow closer to the runner. It was thus very interesting to find the same behavior as early as in the spiral casing. The effect is related to a reduction of the centrifugal force in the boundary layer.

A numerical prediction of the flow in the Hölleforsen guide vane passage is compared with the experimental results. It is shown that the prediction captures the main flow features between the guide vanes and that the separate guide vane computations can be used to generate inlet boundary conditions for computations of the Hölleforsen Kaplan runner.

2.5 Paper V

This paper “*A Numerical Investigation of the Flow in the Wicket Gate and Runner of the Hölleforsen (Turbine 99) Kaplan Turbine Model*”, was presented at the *Turbine 99 - II* workshop in Älvkarleby, Sweden, in 2001. The work presents computational results of the flow in the wicket gate and the runner of the Hölleforsen Kaplan turbine model (see Section 1.2.3). The *Turbine 99* workshops actually study the flow in the draft tube of the Hölleforsen model. This paper however contributed detailed information on the flow that enters the draft tube, which complemented the *Turbine 99* measurements. The computatio-

nal results were validated against some of the detailed measurements of the *Turbine 99* workshops, which shows that the computational results capture the experimental flow well. Conservation of angular momentum was used to verify both the computational and experimental results.

The runner computations reported in the paper obtained the inlet boundary conditions from separate guide vane computations. Two different guide vane inlet boundary conditions were used. All three runner computations presented in the paper included the tip clearance. The hub clearance was included in two of the computations. It was found that an experimental peak in the meridional velocity close to the hub at the inlet to the draft tube was not captured by any of the computations. This contradicts a discussion given in [1], in which it was argued that the peak had its origin in the hub clearance. The present paper argues that the peak originates instead in boundary layer effects that are already present in the spiral casing (see Paper IV). The present paper shows however that the computations have difficulty correctly predicting the flow close to the hub. The computations also have problems close to the axis of rotation after the runner, where there is a vortex rope formation with inherent instability, recirculation and streamline curvature caused by upstream effects of the draft tube bend. In this region the steady periodic flow assumption that was made for the computations is inappropriate.

The paper investigates and visualizes some important flow features to add to the current knowledge of the flow structures in water turbine runners. The tip clearance flow and the tip vortex are investigated particularly. The tip clearance volume flow was determined to be about 1% of the total volume flow and the size and location of the tip vortex were determined by visualization. Smearlines were used to investigate the flow at the runner blade surfaces, and particularly the tip vortex flow features. The flow features and resolution of the runner blade wakes were studied and it was found that it is difficult to capture the sharp gradients of the runner blade wakes. The paper proposes that future studies should investigate the use of a better discretization in the runner blade wake region. The paper discusses the radial velocity component at the inlet to the draft tube, which could not be measured and was found to be very important for the *Turbine 99* draft tube computations. It was found that the inlet radial velocity assumption made at the second workshop was appropriate. The pressure recovery in the draft tube was one of the important quantities studied at the *Turbine 99* workshops. The paper studies the pressure recovery in the axial

part of the diffuser after the runner, which corresponds well with the measurements. This study showed that the wall pressure significantly differs from the cross-sectional averaged pressure owing to the swirling motion of the flow in the axial diffuser.

2.6 Paper VI

This paper “*Validations of Finite Volume CFD Against Detailed Velocity and Pressure Measurements in Water Turbine Runner Flow*”, has been submitted for journal publication. The work presents a validation of the CALC-PMB CFD code against detailed velocity and pressure measurements of both the GAMM Francis runner (see Section 1.2.2) and the Hölleforsen Kaplan runner (see Section 1.2.3). The validations are made at the best efficiency operating condition for both runners and at four off-design operating conditions for the GAMM runner. It is shown that the computational results qualitatively capture the main features of the experimental flow in all cases. The behavior of the computational results is similar for both kinds of water turbines, which shows that experience of computations in water turbines will ultimately give quantitatively correct computational results for this kind of flow. The paper shows that the computational method used in this work is reliable for computations of the flow in water turbine runners.

The paper highlights the similarities and differences in the computations of the two kinds of runners. All computational results agree well with the experimental results except in regions where both the measurement and numerical techniques are inadequate. The GAMM computational results mainly differ from the measurements close to the axis of rotation after the runner. This is particularly true at low mass flow, where a strong unsteady vortex rope was formed in the experimental set-up. Neither the computational assumptions of steady periodic flow nor the experimental method is sufficient in this region of high instabilities and recirculation. Thus better measurement techniques and better numerical methods are both needed to study the flow in this region. The Hölleforsen computations also have problems in capturing the flow details at small radii, i.e. close to the hub and close to the axis of rotation. Experimental visualizations indicated a small recirculation region close to the rotational axis after the runner cone, which makes the steady periodic flow assumption less valid. Effects caused by the bend of the draft tube are also not included in the computations, which could affect the flow at the measurement sections.

The investigations of the Hölleforsen flow show that the runner blade wakes and the pressure recovery in the axial diffuser are qualitatively captured by the computations.

2.7 Paper VII

This paper “*Application of a Momentum-Imbalance Method for Investigating Numerical Accuracy in Swirling Flow*”, has been submitted for journal publication. The work presents a method for investigating discretization errors in swirling flow. The fundamental idea of the method is to investigate the conservation of important equations that are not solved for. When all important aspects of the flow are conserved the computational results can be considered correct. The work focuses on the conservation of a sub-set of the angular momentum equations that is particularly important to swirling flow in water turbines. The method is based on the fact that the discretized angular momentum equations are not necessarily conserved when the discretized linear momentum equations are solved. The method may however be used on any equation that should be conserved in the correct solution, and the application is not limited to water turbines.

One of the major requirements of the method is that the balance of the equation investigated must use exactly the same discretization methods as were used in the CFD solver. The reason for this is that small errors in computing the balance make it impossible to investigate the balance error. This requires that the source code is available. Once the balance over each computational control volume is computed the sum over several computational control volumes yields the balance over the composite control volume, since the fluxes through internal faces cancel. A general way to make this summation is to make a volume integral of the balance density, i.e. the balances divided by the volume of the computational control volume. Using a post-processing tool such as Ensign, the sum over any subdomain can be derived by an element based (constant value in each computational control volume) volume integral of the balance density over the subdomain. The only requirements placed on the post-processing tool are that it can cut out arbitrary parts of the computational domain and compute the volumes of the computational control volumes correctly. The overall balance and volume of the computational domain were conserved in the analysis by Ensign, which shows that no significant errors are introduced in this operation.

The paper presents through-flow investigations of the angular momentum balance error in computations of two Kaplan water turbine runners and a simplified geometry of one of the Kaplan runner ducts. The through-flow investigations are generated by computing the balance error between the inlet and a downstream cross-flow surface that is moved from the inlet to the outlet. The result of this operation shows the balance error distribution in the through-flow direction. The balance error is also investigated as global (all of the computational domain) and local (each computational control volume) error estimators.

The paper shows that the first-order hybrid discretization scheme cannot be used for computations of water turbine runner flow. The global angular momentum balance errors for the hybrid discretization scheme are 14% and 15% for the Kaplan runners. The corresponding errors for the second-order Van Leer scheme are 0.5% and 0.7%. The global imbalances of the hybrid scheme are thus about 30 times larger than for the Van Leer scheme. It may seem that a 0.7% angular momentum balance error for the Van Leer scheme is rather good, but there are at least two reasons why the error should be reduced: 1) the linear momentum is better predicted; 2) water turbine efficiencies are very high (about 95%) and the improvements that can be made are in the range of 0.1% in efficiency. Since the efficiency is closely related to the angular momentum balance it is interesting to further investigate the angular momentum balance for the Van Leer scheme.

2.8 Paper VIII

This paper “*Validations and Investigations of the Computed Flow in the GAMM Francis Runner and the Hölleforsen Kaplan Runner*”, will be presented at the *21st IAHR Symposium* in Lausanne, Switzerland, in 2002. The work presents validations of the CALC-PMB CFD code against experimental observations and detailed measurements of both the GAMM Francis runner (see Section 1.2.2) and the Hölleforsen Kaplan runner (see Section 1.2.3). The computational results are numerically verified using conservation of angular momentum. The computational results qualitatively capture the experimental flow features and the global angular momentum imbalance ranges between 0.5% and 3%.

The predicted flow in the GAMM Francis runner and the Hölleforsen Kaplan runner is investigated to gain a better understanding of the flow in water turbine runners. The flow through the tip clearance of the Hölleforsen Kaplan runner is studied at two operating conditions,

the best efficiency operating condition and a reduced runner speed operating condition. When the runner speed is decreased the load of the runner blades increases and the tip clearance flow increases. The computed flow through the 0.4mm -wide tip clearances of the Hölleforsen runner model is $5.45 \cdot 10^{-3}\text{m}^3/\text{s}$ for the best efficiency operating condition, and $1.69 \cdot 10^{-2}\text{m}^3/\text{s}$ for the low unit speed case (all five runner blades). This corresponds to 1.0% of the total volume flow for the best efficiency operating condition and 3.2% of the total volume flow for the low unit speed case. The tip clearance flow gives rise to a jet on the suction side of the runner blade that interacts with the shroud boundary layer and forms a vortex. Visualization of the flow in the tip vortex shows that it is small for the best efficiency operating condition but is very large for the low unit speed case. The vortex core is close to the runner blade tip at the best efficiency operating condition but is further away from the tip in the low unit speed case. The computed regions of low static pressure are compared to experimentally observed cavitation behavior for a similar runner at roughly the same operating conditions as the computations. In particular the best efficiency predictions agree with the cavitation behavior. The low unit speed experimental observation shows that the tip vortex cavitation starts earlier than at the best efficiency operating condition and that there is a leading edge cavity. This is qualitatively captured by the computations. It should be noted however that the computations are single phase computations that do not take cavitation effects into account.

The paper investigates the use of surface restricted streamlines (smear-lines) to visualize flow features in water turbine runners. Some known computed flow features were easily visualized and numerous new computed flow features were discovered, e.g. separation, re-circulation, reattachment and stagnation. Once the new flow features were discovered they were easily investigated using ordinary streamlines. A combination of both kinds of visualizations gives the best understanding of how the flow behaves.

Chapter 3

Further investigations of the Hölleforsen runner flow

This chapter further investigates the flow at section Ia of test case T of the Hölleforsen model (see Section 1.2.3). The comparisons are thus made at a head of $H = 4.5m$, a runner speed of $N = 595rpm$ and a volume flow rate of $Q = 0.522m^3/s$.

The computational results are compared both to experimental mean values and phase resolved values at section Ia. The following sections describe the measurement techniques, the computational technique and how to compare the experimental and numerical results.

3.1 The measurements

The velocity and corresponding RMS values were measured at the *Turbine 99* [1] and the *Turbine 99 - II* workshops using the LDV technique (Laser Doppler Velocimetry). The technique and its limitations and error sources are thoroughly described by Andersson [2]. The LDV technique measures one instantaneous velocity component (measurement sample) of individual seeding particles that follow the flow through the focus of two laser beams. In this case two orthogonal laser beam pairs were focused at the same measurement control volume, which allows simultaneous measurement of two velocity components, their RMS values and cross correlation. The components measured at section Ia are the axial, which is aligned with the axis of rotation and positive in the main flow direction, and the tangential, which is orthogonal to both the axis of rotation and the radial direction and is positive when the flow is co-rotating with the runner. Since the measurements are made at

a point that is steady in an inertial coordinate system, it is the absolute (inertial) velocities that are measured. Figure 3.1 shows that the measurements were made at two locations, which was done in order to study the tangential variation. Measurement sections Ia(1) and Ia(2) are located at approximately opposite sides of the draft tube cone (section Ia(1) is the same as the official section Ia). Two kinds of velocity measurements at section Ia were presented at the workshops. These are described below.

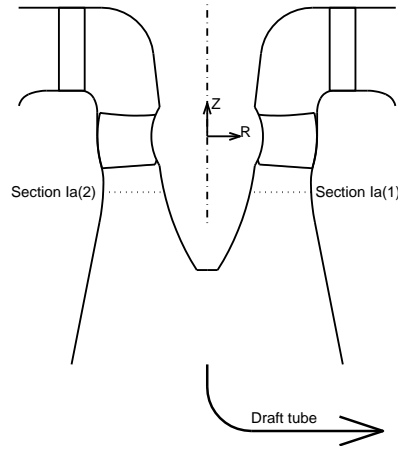


Figure 3.1: The locations of measurement sections Ia(1) and Ia(2). Section Ia(1) is the same as the official section Ia.

At the first workshop the mean axial and tangential velocity components and RMS values were measured as

$$X = \frac{\sum_{i=1}^N x_i \tau_i}{\sum_{i=1}^N \tau_i} \quad (3.1)$$

$$x' = \sqrt{\frac{\sum_{i=1}^N x_i^2 \tau_i}{\sum_{i=1}^N \tau_i} - X^2} \quad (3.2)$$

where x_i is an individual measurement sample, τ_i is the corresponding weight factor (set to $\tau_i = 1$ in all the measurements) and N is the number of measurement samples at each radius. $x_{i=1:N}$ is thus a collection of all the samples of a single instantaneous velocity component from one measurement period that were made at a single radius at section Ia(1) or section Ia(2). X is the weighted mean of $x_{i=1:N}$, computed irrespective of the location of the runner blades. x' is the RMS value (Root Mean Square) of $x_{i=1:N}$, which corresponds to a typical magnitude of

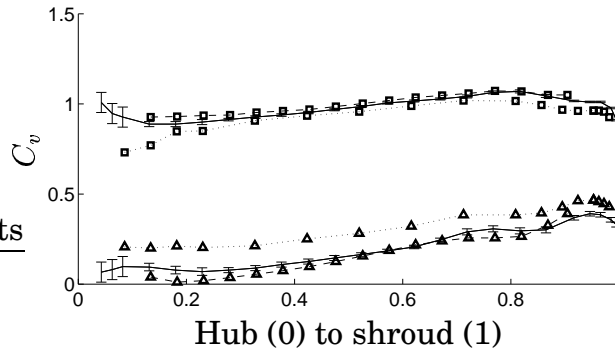
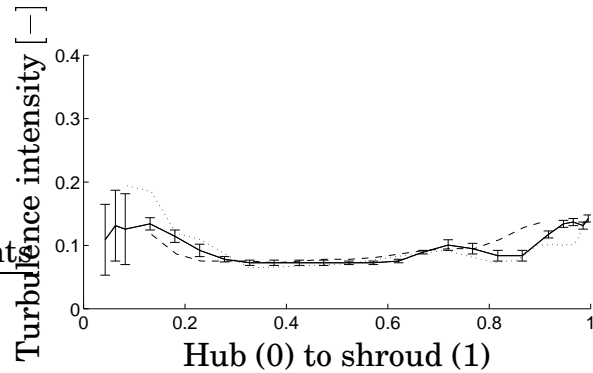


Figure 3.2: Comparison of three velocity measurements at section Ia. Solid lines with error bars: official measurements Ia/Ia(1); dashed lines: Ia(2); dotted lines: tangential average of phase resolved measurements. Measurement markers: \triangle : tangential; \square : meridional.

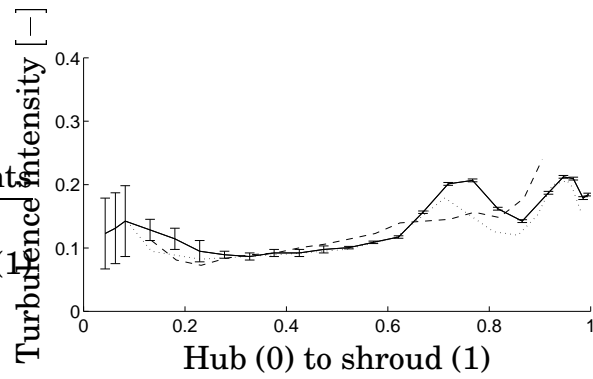
the fluctuation of the velocity component. Since there is a rotating runner above the measurement section, this means that the measurements are circumferentially averaged relative to the runner. It must be kept in mind that X_i and x' include measurement samples that are both inside and outside the runner blade wakes.

Figures 3.2 and 3.3 show the radial distributions of the three different measurements of velocity and RMS profiles of section Ia that were given at the *Turbine 99 - II* workshop. These measurements were made at both sections Ia(1) and Ia(2). At the *Turbine 99 - II* workshop the phase resolved measurements that are also used for these comparisons were made at section Ia(1). The phase resolved measurements are further described below. The values are normalized with $U_{mean} = Q/A_{Ia}$, where $Q = 0.522m^3/s$ is the volume flow and $A_{Ia} = 0.15m^2$ is the cross section area at Ia. The measurements thus indicate a non-negligible tangential variation of 2% and 15% for the average of the meridional and tangential velocity components between section Ia(1) and Ia(2), respectively [1]. The RMS distributions at sections Ia(1) and Ia(2) also indicate a non-negligible tangential variation. This variation has its origin in non-axisymmetric flow conditions at the distributor inlet and upstream effects from the draft tube bend. The non-axisymmetry in the experimental flow must be kept in mind when comparing the computational results with the measurements.

The phase resolved measurements were made at section Ia(1) but at a slightly different operating condition, with about 1% lower mass flow owing to a plexiglass window failure. The original operating condition could not be reproduced since no changes in the experimental set-up



(a) Axial component.



(b) Tangential component.

Figure 3.3: Comparison between the three RMS measurements at section Ia. Solid lines with error bars: official measurements Ia/Ia(1); dashed lines: Ia(2); dotted lines: tangential average of phase resolved measurements.

could be found. This sensitivity to small changes in the operating condition must be kept in mind when comparing the computational results with the measurements.

At the second workshop the **phase resolved** distribution of the axial and tangential velocity components and RMS values were measured as

$$X(\theta_r) = \frac{\sum_{i=1}^N x_i \tau_i}{\sum_{i=1}^N \tau_i} \Bigg|_{\theta_r \pm \Delta\theta_r/2} \quad (3.3)$$

$$x'(\theta_r) = \sqrt{\frac{\sum_{i=1}^N x_i^2 \tau_i}{\sum_{i=1}^N \tau_i} \Bigg|_{\theta_r \pm \Delta\theta_r/2} - X^2(\theta_r)} \quad (3.4)$$

where x_i is an individual measurement sample, τ_i is the corresponding weight factor (set to $\tau_i = 1$ in all the measurements) and N is the number of measurement samples at each tangential angle (phase compartment), $\theta_r \pm \Delta\theta_r/2$, relative to the runner. $x_{i=1:N}$ is thus a collection of all the samples of a single instantaneous velocity component from one measurement period that were made at a single radius and a single phase compartment, $\theta_r \pm \Delta\theta_r/2$, at section Ia(1). For each radius the measurements thus give $X(\theta_r)$, which is the phase-average of the velocity component at $\theta_r \pm \Delta\theta_r/2$, and $x'(\theta_r)$, which is its corresponding phase averaged RMS value. Both $X(\theta_r)$ and $x'(\theta_r)$ thus resolve the runner blade wakes if $\Delta\theta_r$ is sufficiently small. On the other hand, $\Delta\theta_r$ must also be large enough to contain a sufficient number of measurement samples. $\Delta\theta_r = 2\pi$ gives the same kinds of measurements as were made for the first workshop.

Since the variation between the flow after each runner blade was negligible the measurements samples from all blade passages were averaged relative to a single blade passage, which increased the number of samples in each $\Delta\theta_r$ five times (five runner blades). The results were then copied periodically for the visualization. These experimental results are shown below in comparison with the computational results.

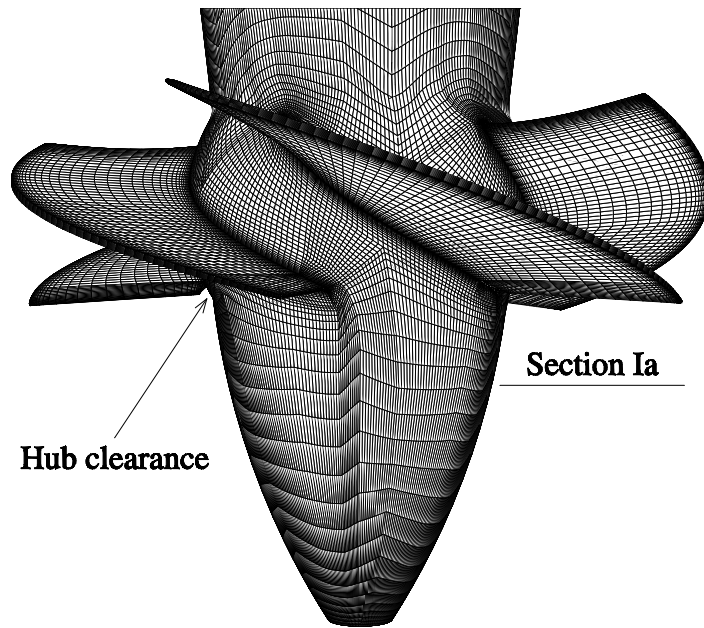
3.2 The computations

The Hölleforsen flow is predicted in both the wicket gate and the runner. The computations are made in two steps [17]. The flow in the wicket gate is first computed, using a fully developed turbulent 1/7

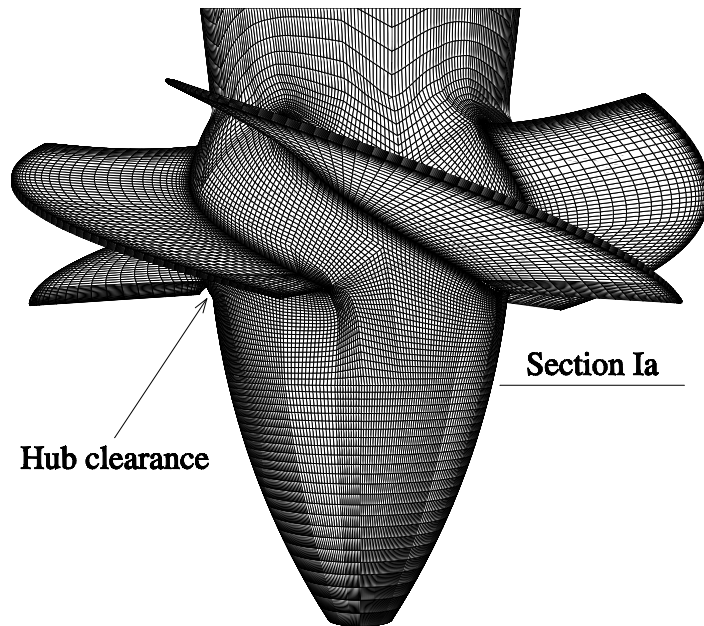
profile as the inlet boundary condition. The computed flow in the wicket gate shows good agreement with observations [15] and the choice of wicket gate inlet boundary condition does not seem to be important for the flow at section Ia [17]. The wicket gate computational result is circumferentially averaged and applied as the inlet boundary condition for the runner computations.

All computations are made for the steady periodic flow in a single blade passage. The computational coordinate system is fixed to the blade, which is non-rotating in the case of a guide vane and rotating in the case of a runner blade. The computational grid for a single guide vane passage consists of 285 177 control volumes, while three different grids are used for the runner computations. The runner computational cases are named after their grids, since this is the only feature that distinguishes them. Figure 3.4 shows the three grids and their main differences. Grid 1 was used for the **standard** case in the contribution to *Turbine 99 - II* [17]. The grid for a single runner blade passage consists of 722 157 control volumes. 15 884 control volumes are in the tip clearance, where 19 control volumes are in the runner blade tip to shroud direction. 2 926 control volumes are in the hub clearance at the trailing edge close to the hub. Grid 2 is basically the same as grid 1, but the number of control volumes in the axial direction between the runner blades and the end of the hub is doubled (104 328 extra control volumes). Grid 3 is basically the same as grid 2, but the grid lines between the runner blades and section Ia are approximately aligned with the main flow direction (with respect to the velocities relative to the rotating coordinate system). The grid lines below section Ia could unfortunately not be aligned with the main flow direction since the conservation of angular momentum makes the control volumes extremely skew. Grid 3 introduces major numerical convergence problems, which increases the computational cost. This grid was developed to show the effect of grid distribution versus grid density, but it is not an option for quick computational results.

The grid density is thus the same for grids 2 and 3, but the grid distributions differ. Grids 1 and 2 include the hub clearance at the trailing edge of the runner blade, which is not included in grid 3. The inclusion of an extra structured block in the hub clearance affects the grid distribution outside the clearance as well, but computations made without the hub clearance using grids that were and grids that were not prepared for the inclusion of hub clearance show that this does not affect the computational results. Grid 3 is not prepared to include the hub clearance, which has a positive effect on the convergence rate.

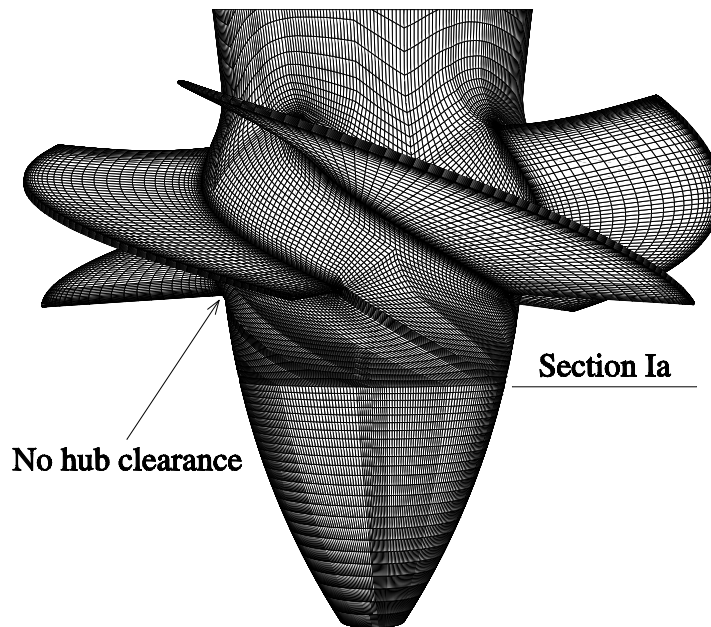


(a) Grid 1.



(b) Grid 2.

Figure 3.4: Continued...



(c) Grid 3.

Figure 3.4: ...continued. The three grids used to compare the grid dependency on the prediction of the flow at section Ia. The main differences between the grids are the grid density and the grid distribution between the runner blades and section Ia. Grid 1 and grid 2 include the hub clearance, which is not included in grid 3. Note that the flow in only one blade passage is computed, employing periodic boundary conditions.

The computational results basically give the three relative Cartesian velocity components, the static pressure, the turbulent kinetic energy ($k = 1/2\overline{u_i u_i}$) and the specific dissipation (ω), at the center of all the computational control volumes.

3.3 How to compare the computational results with the measurements

To be able to compare the computational results with the measurements it must be certain that the correct quantities are compared. Focusing on a single point in the inertial coordinate system, one can decompose the instantaneous absolute (inertial) velocity component, u_a , as

$$u_a = \langle u_a \rangle + u'_a = U_a + \tilde{u}_a + u'_a \quad (3.5)$$

where

$$\langle u_a \rangle = U_a + \tilde{u}_a \quad (3.6)$$

is its phase average, U_a is its mean value, \tilde{u}_a is its phase averaged deviation from the mean value and u'_a is its deviation from the phase average owing to turbulent (stochastic) motions. By the definitions, we have

$$\begin{aligned} \langle u'_a \rangle &= 0 \\ \langle \langle u_a \rangle u'_a \rangle &= 0 \\ \langle \langle u_a \rangle \rangle &= \langle u_a \rangle \\ \langle \tilde{u}_a \rangle &= \tilde{u}_a \\ \langle U_a \rangle &= U_a \\ \langle \langle U_a \rangle u'_a \rangle &= 0 \end{aligned}$$

Investigating the phase average of the square of the instantaneous velocity component, we have from equation 3.5

$$\begin{aligned} \langle u_a^2 \rangle &= \langle (\langle u_a \rangle + u'_a)^2 \rangle \\ &\Rightarrow \langle u_a^2 \rangle = \langle u_a \rangle^2 + \langle u'_a u'_a \rangle + 2\langle \langle u_a \rangle u'_a \rangle \\ &\Rightarrow \langle u_a^2 \rangle - \langle u_a \rangle^2 = \langle u'_a u'_a \rangle \end{aligned} \quad (3.7)$$

Defining an average over all phases, such as

$$\widehat{u}_a = U_a \quad (3.8)$$

we have

$$\begin{aligned}\widehat{\tilde{u}_a} &= 0 \\ \widehat{u'_a} &= 0 \\ \widehat{U_a} &= U_a \\ \widehat{\langle u_a \rangle} &= U_a \\ \widehat{U_a \tilde{u}_a} &= 0\end{aligned}$$

Applying this averaging technique to equation 3.7 yields

$$\begin{aligned}\widehat{\langle u_a^2 \rangle} - \widehat{\langle u_a \rangle^2} &= \widehat{\langle u'_a u'_a \rangle} \\ \Rightarrow \widehat{\langle u_a^2 \rangle} - \widehat{(U_a + \tilde{u}_a)^2} &= \widehat{\langle u'_a u'_a \rangle} \\ \Rightarrow \widehat{\langle u_a^2 \rangle} - U_a^2 - \widehat{\tilde{u}_a \tilde{u}_a} - 2\widehat{U_a \tilde{u}_a} &= \widehat{\langle u'_a u'_a \rangle} \\ \Rightarrow \widehat{\langle u_a^2 \rangle} - U_a^2 &= \widehat{\langle u'_a u'_a \rangle} + \widehat{\tilde{u}_a \tilde{u}_a}\end{aligned}\tag{3.9}$$

Equations 3.6 - 3.9 describe how to compare the computational results with the measurements. Equations 3.6 and 3.8 describe how to compare the velocity distributions and equations 3.7 and 3.9 describe how to compare the RMS distributions.

Letting the left hand side of equation 3.6 be the measurements, we have (c.f. equation 3.3)

$$\langle u_a \rangle_{\theta_r \pm \Delta\theta_r/2} = \frac{\sum_{i=1}^N u_a \tau_i}{\sum_{i=1}^N \tau_i} \Big|_{\theta_r \pm \Delta\theta_r/2}$$

where the terms are evaluated in a phase compartment $\theta_r \pm \Delta\theta_r/2$ relative to the runner. The right hand side of equation 3.6 is exactly what is resolved by the computations, which give the steady velocity distribution (including spatially periodic fluctuations) at all locations relative to the runner. The computed relative velocity must however be converted to absolute velocity by subtracting the solid body rotation of the computational coordinate system.

Equation 3.8 is the mean velocity (c.f. equation 3.1), measured as

$$\widehat{u_a} = \frac{\sum_{i=1}^N u_a \tau_i}{\sum_{i=1}^N \tau_i}$$

This can be obtained as a tangential spatial mean of the computed steady velocity distribution, converted to absolute velocity by subtracting the solid body rotation of the computational coordinate system.

Letting the left hand side of equation 3.7 be the measurements, we have (c.f. equations 3.3 and 3.4)

$$\langle u_a^2 \rangle_{\theta_r \pm \Delta\theta_r/2} - \langle u_a \rangle_{\theta_r \pm \Delta\theta_r/2}^2 = \left. \frac{\sum_{i=1}^N u_a^2 \tau_i}{\sum_{i=1}^N \tau_i} - \left(\frac{\sum_{i=1}^N u_a \tau_i}{\sum_{i=1}^N \tau_i} \right)^2 \right|_{\theta_r \pm \Delta\theta_r/2}$$

This is exactly the square of equation 3.4, which is the RMS of the measurements. The right hand side of equation 3.7 can be obtained from the computations. Since the computations are steady it is exactly the phase average relative to the runner that is computed. The coordinate system has a constant rotation, which does not influence the fluctuating velocity since the fluctuating velocity cannot contribute to the mean velocity, yielding

$$\langle u'_a u'_a \rangle_{\theta_r \pm \Delta\theta_r/2} = \langle u'_r u'_r \rangle_{\theta_r \pm \Delta\theta_r/2}$$

where r denotes the relative velocity. The phase average at $\theta_r \pm \Delta\theta_r/2$ in the inertial coordinate system is the same as the time average at $\theta_r \pm \Delta\theta_r/2$ in the rotating coordinate system, yielding

$$\langle u'_r u'_r \rangle_{\theta_r \pm \Delta\theta_r/2} = \overline{u'_r u'_r} \Big|_{\theta_r \pm \Delta\theta_r/2}$$

From the computations, the Boussinesq hypothesis gives the Reynolds stress tensor in the rotating coordinates as

$$\overline{\rho u'_i u'_j} = -\mu_t \left(\frac{\partial U_i}{\partial x_j} + \frac{\partial U_j}{\partial x_i} \right) + \frac{2}{3} \delta_{ij} \rho k$$

where U_i are the mean relative velocity components, u'_i are the turbulent fluctuating components and k is the turbulent kinetic energy.

However, the measured values are the Cartesian components relative to the inertial coordinate system, while it is the Cartesian components relative to the rotating coordinate system that are computed. The computed Reynolds stress tensor must then be tensor-rotated for different phases. The tensor rotation [13] between two Cartesian coordinate systems is described by the transformation tensor, $a_{ij} = \cos(x'_i, x_j)$, where $\cos(x'_i, x_j)$ is the cosine of the angle between the i th primed and j th unprimed coordinate axes. A Cartesian tensor in the unprimed coordinate system can then be transformed to the primed coordinate system as

$$T'_{ij} = a_{ip} a_{jq} T_{pq}$$

Turning our attention to equation 3.9, the second term on the left hand side is measured as (c.f. equation 3.1)

$$U_a^2 = \left(\frac{\sum_{i=1}^N u_a \tau_i}{\sum_{i=1}^N \tau_i} \right)^2$$

The first term, $\overline{\langle u_a^2 \rangle}$, is however not as obvious as the second term. We want it to be equal to the measured quantity

$$\widehat{u_a^2} = \frac{\sum_{i=1}^N u_a^2 \tau_i}{\sum_{i=1}^N \tau_i} \quad (3.10)$$

to get (c.f. equation 3.2)

$$\overline{\langle u_a^2 \rangle} - U_a^2 = \frac{\sum_{i=1}^N u_a^2 \tau_i}{\sum_{i=1}^N \tau_i} - \left(\frac{\sum_{i=1}^N u_a \tau_i}{\sum_{i=1}^N \tau_i} \right)^2$$

Since the instantaneous velocity in the inertial coordinate system is a function of time in reality, the exact mean of the square of the instantaneous velocity is obtained from the integral

$$\widehat{u_a^2} = \frac{1}{T} \int_T u_a^2 dt \quad (3.11)$$

Grouping the integral into N time phases, ΔT , that have equal size in time ($T = N\Delta T$), we get

$$\widehat{u_a^2} = \frac{1}{N} \left(\frac{1}{\Delta T} \int_{\Delta T_1} u_a^2 dt + \frac{1}{\Delta T} \int_{\Delta T_2} u_a^2 dt + \dots + \frac{1}{\Delta T} \int_{\Delta T_N} u_a^2 dt \right)$$

which is the arithmetic mean of the phase averaged quantity. For discrete measurements it can be shown (starting with equation 3.10 instead of equation 3.11) that the weight of the phases must be the same or, if $\tau_i = 1$, the number of measurement samples in each phase must be the same. The precision of the phase resolved measurements thus increases with the total number of samples, since the imbalance between the phases is reduced. Ideally, for phases of equal size, we thus have

$$\overline{\langle u_a^2 \rangle} = \widehat{u_a^2}$$

The right hand side of equation 3.9 can easily be derived from the computations as circumferential averages of the computational results.

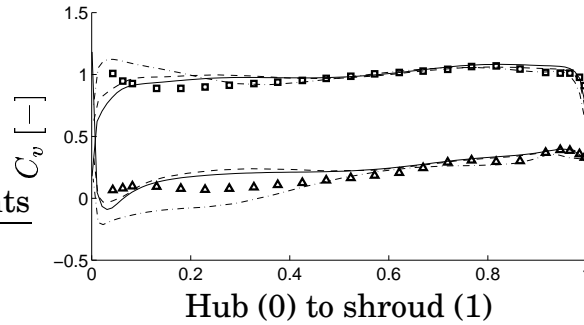


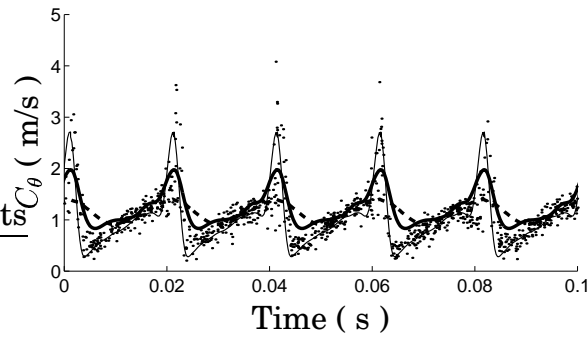
Figure 3.5: Comparison between computed and measured velocity coefficient distributions at section Ia. Solid lines: grid 1; dashed lines: grid 2; dashed-dotted lines: grid 3. Measurement markers: \triangle : tangential; \square : meridional.

3.4 Comparisons at section Ia

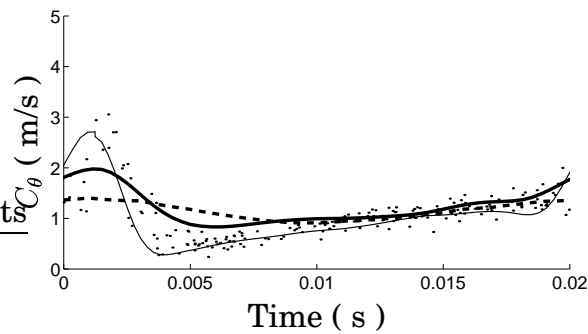
Figure 3.5 shows a comparison between the velocities of the circumferentially averaged computational results and the measurements at section Ia (velocities made dimensionless with $U_{mean} = Q/A_{Ia}$, where $Q = 0.522m^3/s$ and $A_{Ia} = 0.15m^2$). Grids 1 and 2 give approximately the same results, while the results from grid 3 differ in the half channel width closest to the hub. The result from grid 3 resolves a meridional velocity peak close to the hub that could not be resolved with the other grids. Andersson [1] argued that this peak originates in the leakage between the runner hub and the runner blades. However, grids 1 and 2 include this leakage and do not resolve a peak, while grid 3 does not include the leakage but resolves a peak. It is thus more likely that this effect originates in boundary layer effects already present at the inlet of the wicket gate [15, 17]. The tangential velocity of grid 3 close to the hub seems however to be reduced too much as compared with the experiment.

The computations resolve the periodic behavior of the wake at section Ia, as shown by Andersson [1]. However, it is important to have sufficiently small computational control volumes in the wake region. The computations are unable to predict the sharp wake peaks when the control volumes in the wake region are too large, yielding a more sinusoidal behavior (figure 3.6, grid 1). The wake is captured qualitatively if the grid resolution in the wake region is refined (grid 2), and if the grid lines are aligned with the main flow the wake is captured even better (grid 3).

Figure 3.7 compares the computed and measured turbulence inten-

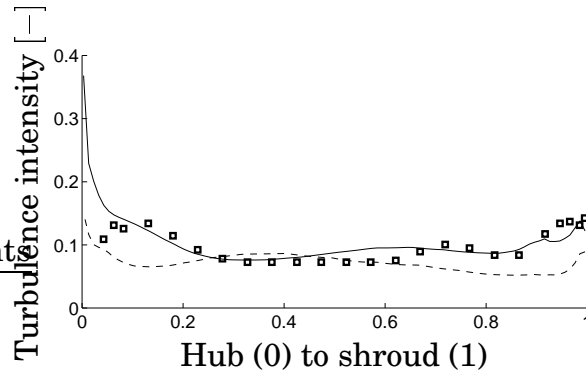


(a) Five runner blade passages.

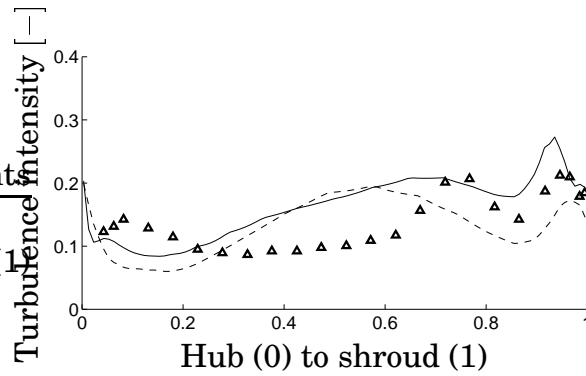


(b) Zoom of the first runner blade passage.

Figure 3.6: Comparison between computed and measured periodic behavior of the tangential velocity component at $r^* = r/R = 0.92$ at section Ia. Dots: individual measurement samples; dashed line: grid 1; thick solid line: grid 2; thin solid line: grid 3. The computational results have been phase-shifted to match the measurements because it was not possible to obtain the exact runner angles of the measurements. One runner revolution (five blades passages) takes approximately 0.1s.



(a) Axial component.



(b) Tangential component.

Figure 3.7: Comparison between the computational results and the original measurements at section Ia with respect to turbulence intensity. Dashed lines: grid 2; solid lines: grid 3. Measurement markers: \square : axial; \triangle : tangential.

sities (RMS values made dimensionless with $U_{mean} = Q/A_{Ia}$) at section Ia. The axial component is best captured by computations using grid 3, while the tangential component is captured less accurately by both grids 2 and 3. However, both grids qualitatively capture the first maxima and minima in the tangential component close to the shroud.

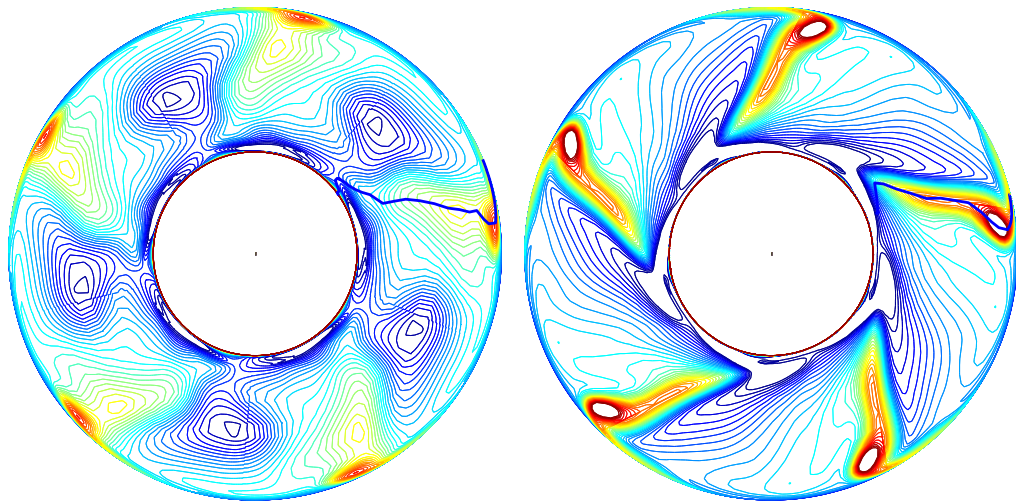
Figures 3.8 and 3.9 compare the measured and computed phase resolved velocities at section Ia. It should be noted that the computational results have been rotated to the same angle (relative to the runner) as the measurements and that both the experimental and the computational results are copied periodically for the visualization. Grids 2 and 3 both capture the distribution of the runner blade wake, which is marked by a thick solid line in the plots. The runner blade wake is defi-

ned as the location of the maximum tangential velocity for each radius. The wake is sharp in both the measurements and the computational results from grid 3. The wake is too smeared out in grid 2, however, since the main flow in the wake region is diagonally through the control volumes, which introduces numerical diffusion. It should be noted that there is a slight difference in operating conditions between the computations and the measurements, which gives a difference in the levels of the tangential component between the computations and the measurements. The computational result from grid 3 qualitatively predicts the same tangential velocity distribution as the measurements, but the lowest velocity is lower and the highest velocity is higher than for the measurements. The computed axial components show some similarities with the measurements, but the differences overshadow these.

It should be noted that it was not possible to make measurements all the way to the hub because of reflections of the laser beams that disturbed the signal. A circle marks the hub width in the measurement plots. The measurements made closest to the hub (the region with rugged tangential contour lines) show that the signal is disturbed far out into the flow. The measured low (blue) axial velocity contour lines are therefore questionable. On the other hand, the two computations do not agree if the axial flow in this region is low or high. All computations of this case show that it is particularly difficult to predict the flow close to the hub.

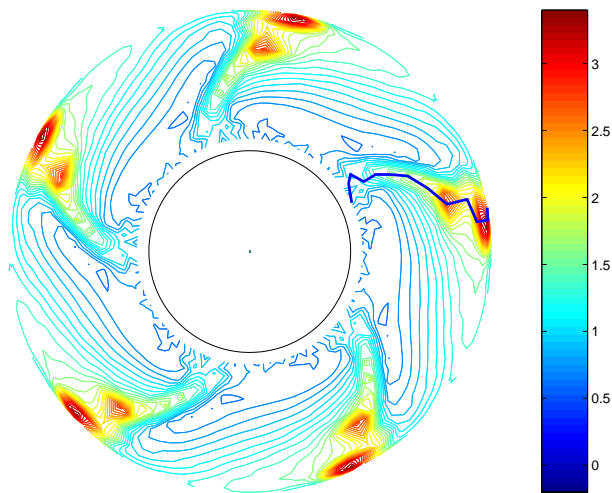
The effect of the tip vortex can be seen as a local increment in the tangential velocity and a local reduction in the axial velocity in the runner blade wake close to the shroud. The measurements have two local maxima in the tangential component, however, while the computations have only one. The second maxima might originate in effects that are not included in the computations, such as the guide vane wakes.

Figures 3.10 and 3.11 show a comparison between the RMS distributions of the phase resolved measurements and the computations. It should once again be noted that the computational results have been rotated to the same angle (relative to the runner) as the measurements and that both the experimental and the computational results are copied periodically for the visualization. The runner blade wake is shown as a thick solid line. As for the velocity components, the wake is too smeared out for grid 2. Grid 3 however resolves the sharp gradients of the wake. The effect of the tip vortex can clearly be seen in the local increment in the tangential and the axial RMS components below the wake line close to the shroud, both in the results from grid 3 and in the measurements. It is also interesting to see that the Boussinesq as-



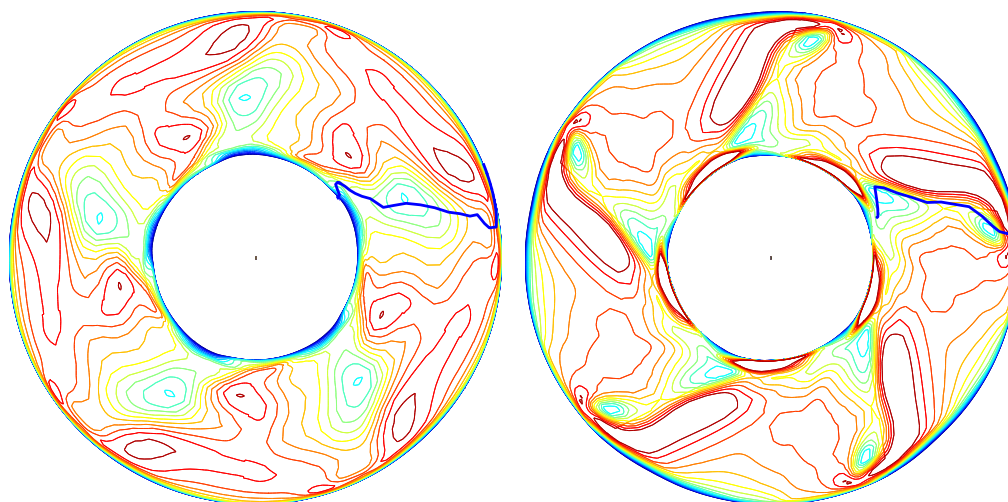
(a) Computed tangential velocity, grid 2.

(b) Computed tangential velocity, grid 3.



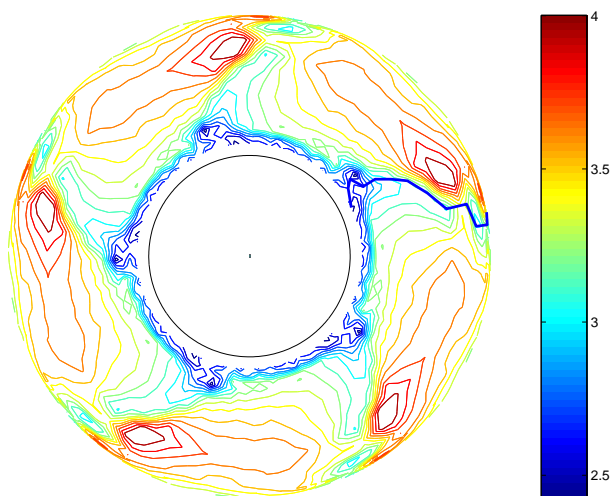
(c) Measured tangential velocity.

Figure 3.8: Comparison between the computed tangential velocity and the phase resolved measurements at section Ia. The equidistance is $0.1m/s$ and the color scale is the same for the measurements and the computations.



(a) Computed axial velocity, grid 2.

(b) Computed axial velocity, grid 3.



(c) Measured axial velocity.

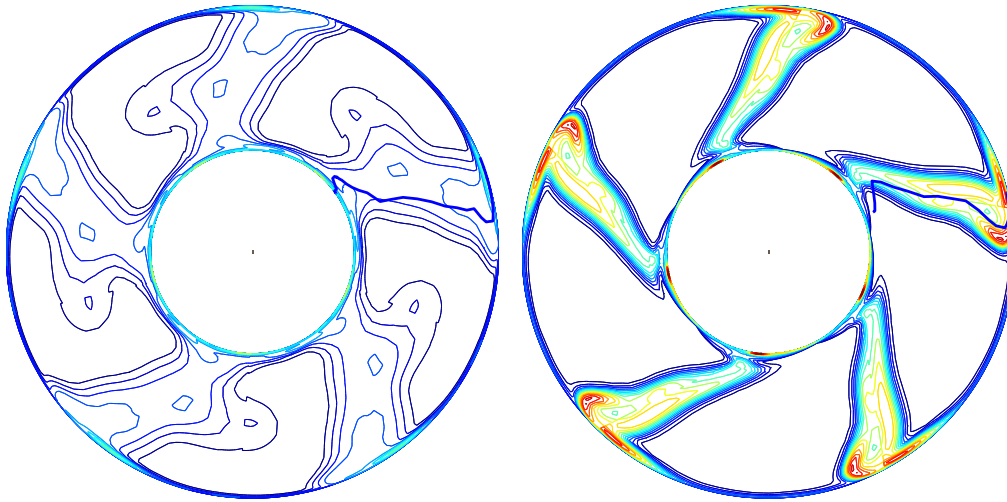
Figure 3.9: Comparison between the computed axial velocity and the phase resolved measurements at section Ia. The equidistance is $0.1m/s$ and the color scale is the same for the measurements and the computations.

sumption predicts a non-negligible anisotropic turbulence although the $k - \omega$ turbulence model is based on the assumption of isotropic turbulence. As for the velocities, the measured RMS values closest to the hub are disturbed by light reflections, which makes them questionable. On the other hand, it is also particularly difficult to predict the flow close to the hub as already mentioned. It should be noted that grid 3 does not include the hub clearance, which would increase the turbulence level close to the hub. This cannot be seen in the results from grid 2, since that wake is too smeared out, but it has been observed in preliminary computations with a grid similar to grid 3 but which included the hub clearance.

Figure 3.12 shows that the overall pattern of the RMS distributions can be found in the computed turbulent kinetic energy from the k -equation. The tip vortices thus contain high turbulent kinetic energy, which contributes to a reduction of the efficiency of the machine.

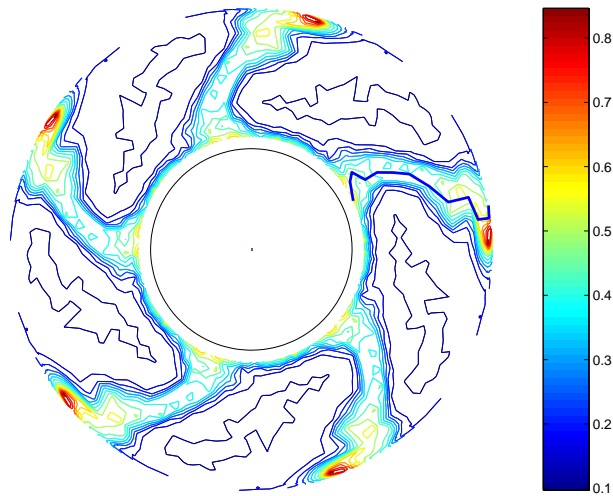
3.5 Comments to the phase resolved comparisons

The computational results in this section show that the grid lines should be aligned with the flow to resolve the runner blade wakes and produce good phase resolved results. Grid distribution is much more important than grid density in this case. This is not surprising. It is in fact rather obvious, since the flow below the runner blades goes diagonally through the control volumes in grids 1 and 2, which introduces numerical diffusion and smears out the wake, while grid 3 preserves the wake down to section Ia. However, aligning the grid lines with the flow in a water turbine is a difficult task that requires an iterative procedure with re-meshing or an adaptive grid method. When a block structured grid is used the control volumes tend to become extremely skew, as in grid 3, which introduces numerical convergence problems. It may also be impossible to generate a good grid, as is the case below section Ia. Grid 3 is thus not the solution to the problem. It is merely a tool to show the effect of grid distribution. It should be recalled that the flow in a real water turbine has wakes from stay vanes and guide vanes that are moving relative to the runner. The wakes from the stay vanes, guide vanes and runner blades are convected into the draft tube, and they are definitely not steady relative to the draft tube. The computational grid must thus in reality resolve wakes everywhere and the computa-



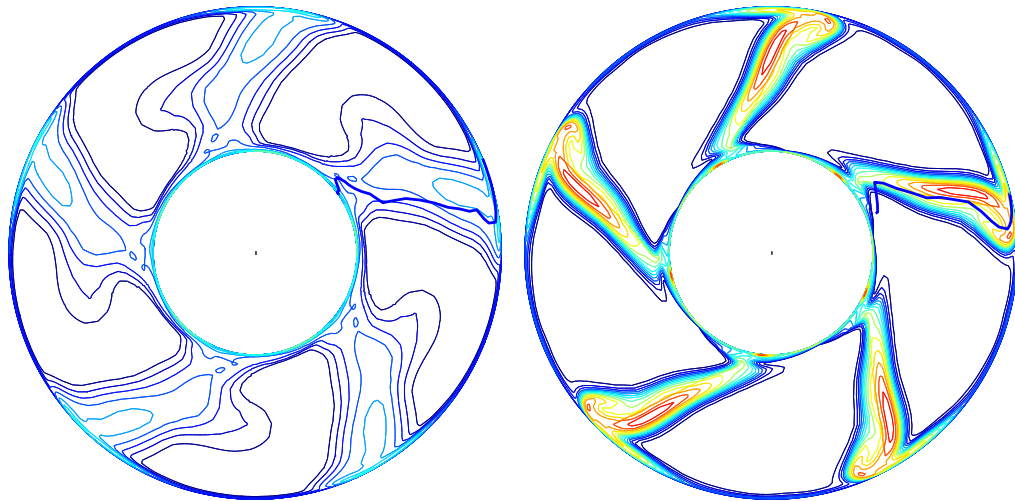
(a) Computed tangential RMS, grid 2.

(b) Computed tangential RMS, grid 3.



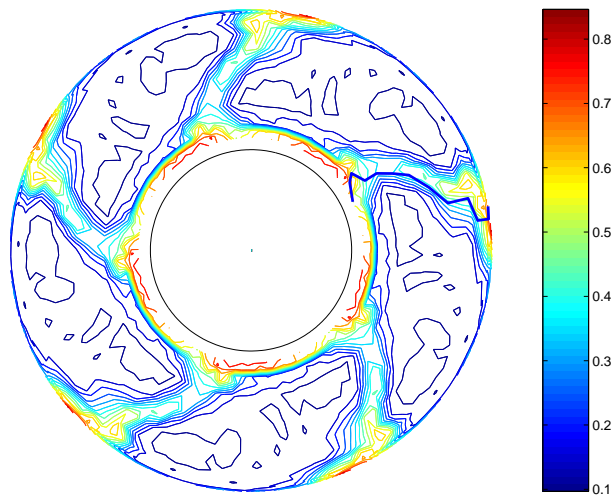
(c) Measured tangential RMS.

Figure 3.10: Comparison between the computed RMS of the tangential velocity component and the phase resolved measurements at section Ia. The equidistance is $0.05m/s$ and the color scale is the same for the measurements and the computations.



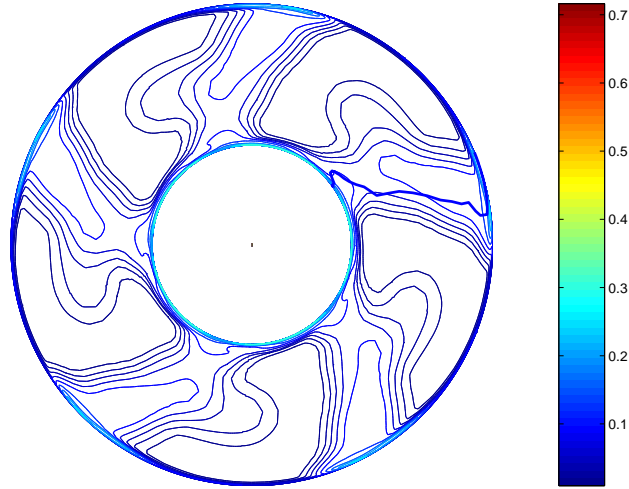
(a) Computed axial RMS, grid 2.

(b) Computed axial RMS, grid 3.

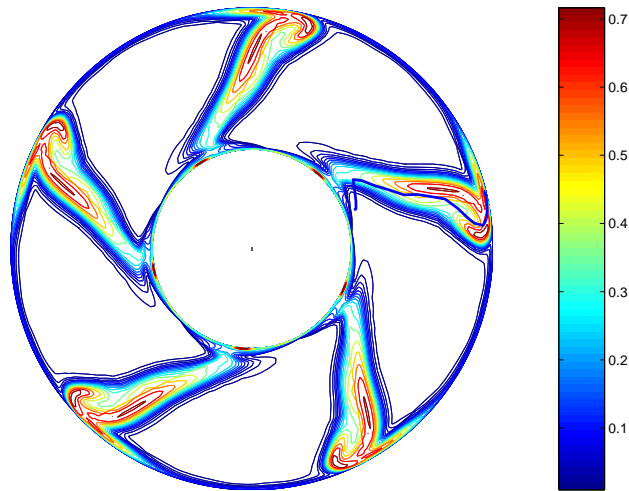


(c) Measured axial RMS.

Figure 3.11: Comparison between the computed RMS of the axial velocity component and the phase resolved measurements at section Ia. The equidistance is $0.05m/s$ and the color scale is the same for the measurements and the computations.



(a) Computed turbulent kinetic energy, grid 2.



(b) Computed turbulent kinetic energy, grid 3.

Figure 3.12: Comparison between the computational results at section Ia with respect to turbulent kinetic energy. Thick solid lines mark the location of the wake (the maximum tangential velocity for each radius). The equidistance is $0.0025m^2/s^2$ and the color scale is the same for both grids. Note that the computational results are copied periodically for the visualization.

tions must include unsteady effects. Neither of these requirements is accounted for in state of the art water turbine computations because of the unreasonable demand for computational power and the need of quick engineering results. The rapid development of computational power is however promising with respect to more detailed and accurate numerical computations of the flow in water turbines.

Higher-order discretization schemes would be another way to increase the accuracy of the computations. Unfortunately, by increasing the order of the discretization scheme, the numerical convergence problems also increase drastically. The solution to this problem has yet to be found.

Chapter 4

Unsteady computations of the Hölleforsen runner flow

This chapter investigates the applicability of unsteady Reynolds averaged Navier Stokes (URANS) computations in the Hölleforsen model runner (see Section 1.2.3). An unsteady computation is applied to predict the interaction between the guide vane wakes and the runner blade tip vortices. The computation is made at the Hölleforsen *standard* operating condition [1, 17] (test case T at the Turbine 99 workshop, which is close to best efficiency).

The method used for the unsteady computation is closely related to the method used for the steady computations. The steady flow in the distributor is first computed including the bend of the channel but without the runner blades, i.e. exactly as for the steady computations. The inlet boundary condition for the unsteady runner computation is then obtained from the distributor computational result at the runner inlet. The inlet boundary condition is thus not circumferentially averaged, but it is periodic in the tangential direction with a periodicity corresponding to the guide vane spacing. The non-axisymmetric inlet boundary condition is counter-rotated at the runner rotational speed during the computations. The wakes of the guide vanes thus give an unsteady inlet boundary condition relative to the runner coordinate system.

The unsteady terms of the Reynolds averaged Navier Stokes equations in the rotating coordinate system are kept to account for the unsteady effects. The second order upwind Van Leer scheme is used for the spatial discretization, and an implicit scheme is used for the time discretization. The time weighting parameter is set to $\theta = 0.7$ for reasons of numerical stability, which means that the time discretization

scheme is slightly more implicit than the true second order Crank-Nicolson scheme, where $\theta = 0.5$. The time step is $8 \cdot 10^{-6} s$ to obtain sufficiently small CFL numbers.

4.1 The unsteady inlet boundary condition

The inlet boundary condition for the unsteady runner computation is obtained from a separate steady computation of the distributor. This method neglects upstream effects of the runner blades on the flow at the guide vanes. LDV measurements of the flow between the guide vanes have shown that this effect is small compared with the turbulent fluctuations [15]. The present implementation requires that both the distributor and runner computational domains have a grid plane at the inlet of the runner computational domain and that the grids match in the cross-channel direction. The grids do not have to match in the tangential direction, since the inlet boundary condition is rotating, which requires a general method to apply the information from the distributor. It should be recalled that there are 24 guide vanes. Since only one guide vane passage is computed, the distributor result is periodic over $360/24 = 15$ degrees. There are however five runner blades and, since only one runner blade passage is computed, the runner flow and its inlet boundary condition must be periodic over $360/5 = 72$ degrees. The present implementation keeps the distribution from the distributor but changes its periodicity to $360/25 = 14.4$ degrees so that there are five guide vanes per runner blade ($5 \cdot 14.4 = 72$). This preserves the mass flow from the distributor result, although the tangential gradients are slightly sharpened.

The 2D distribution of a single guide vane result at the inlet of the runner computational domain is saved in a file that is subsequently read in the runner computation. The solid body rotation of the runner coordinate system is subtracted from the velocity but the scalars are unaffected by the transformation. The tangential distribution of each variable at each location in the cross-channel direction is interpolated using a 1D cubic spline interpolation scheme [19] and copied five times to match the tangential width of the inlet of the runner computational domain. The cubic spline interpolation scheme is smooth in the first derivative and continuous in the second derivative, which preserves the accuracy in the non-matching tangential direction.

At the start of each time step a new inlet boundary condition is interpolated from the distributor result. A periodic time variable is used

together with the runner rotation, Ω , to determine the rotation of the inlet boundary condition. The periodic time variable starts at zero, adds each time step and restarts at zero when it reaches $2\pi/\Omega$. The reason for this is to avoid cancellation when adding small time steps to large times, which would stop the time propagation.

Figure 4.1 shows the runner inlet distribution of the tangential velocity at a single time step. Since the runner is computed in a rotating coordinate system and the distributor results belong to an inertial coordinate system, this boundary condition is rotated opposite to the runner rotation with the same rotational speed as the runner. The runner inlet boundary condition is thus close to axi-symmetric in the upper part and periodic in the lower part. It is however questionable whether the guide vane wakes are properly resolved, since the flow after the guide vanes goes diagonally through the control volumes, which introduces numerical diffusion that smears out the wakes. The wakes are best resolved in the lower part of the inlet, where the control volumes are smallest and the distance between the guide vanes and the inlet of the runner computational domain is smallest. The flow in the upper part between the guide vanes and the runner inlet goes through larger control volumes and, because of conservation of angular momentum, also goes through a larger number of control volumes, which smears out the wakes. The wakes are most likely smeared out in the experimental set-up as well, but the visual access of the model does not allow measurements in this region [15]. The purpose of this work is to study the unsteady effect of the guide vane wakes on the tip vortex flow, and the flow in the tip vortex has its origin in the lower part of the runner inlet, where the wakes are best resolved. The present inlet boundary condition is therefore considered sufficient for preliminary studies of unsteady computations of the runner flow.

4.2 Preliminary results

As previously mentioned, the guide vane wakes are smeared out as they pass diagonally through control volumes that are too large. This problem does not end at the runner inlet. On the way between the runner inlet and the runner blade the wakes pass through numerous such control volumes. The problem is that a grid resolution that resolves the wakes in all of the runner computational domain cannot be afforded, and the grid lines cannot be aligned with the main flow direction. Figure 4.2 shows an instantaneous tangential distribution of the

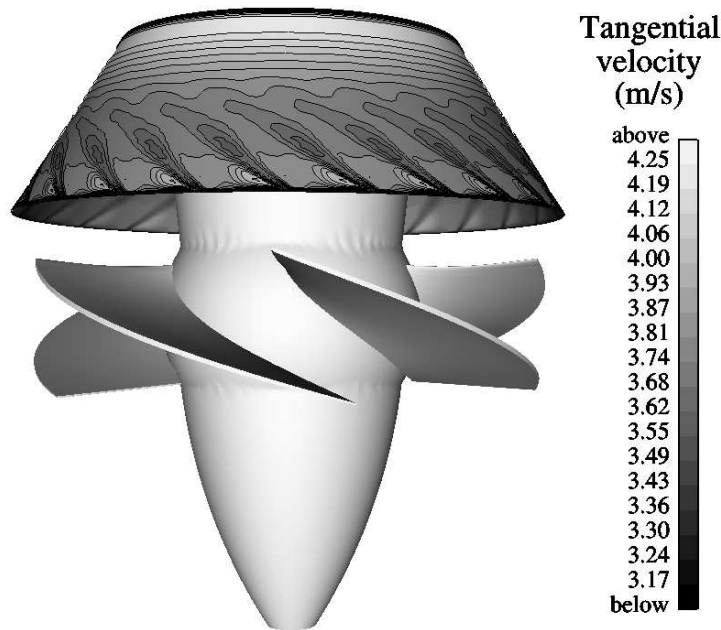


Figure 4.1: Instantaneous isolines of the tangential velocity at the inlet of the runner computational domain.

tangential velocity at 5% of the channel width from the shroud (at radius $r = r_{max} - 0.05(r_{max} - r_{min})$). The distribution is shown at the runner inlet and halfway to the runner blade tip, and for both the runner computational result and the guide vane computational result. The guide vane computational result has no upstream effect of the runner, but it was possible to afford making the grid in the important region slightly finer than for the runner, and the relative velocities are much lower. The flow in the distributor result thus goes through finer control volumes and not as many control volumes as in the runner computations.

The guide vane wakes are very distinct at the runner inlet, but halfway between the runner inlet and the runner blade tip the wakes are smeared out for both the distributor computation and the runner computation, to the greatest extent for the latter. There is an additional periodicity in the runner computation that relates to the runner blade spacing, which is an upstream effect of the runner blades. This periodicity is more or less steady relative to the runner blades, while the higher frequency periodicity from the guide vane wakes move at each time step. The predicted flow at the runner blade tip thus varies more or less sinusoidally with an amplitude that is most likely too low.

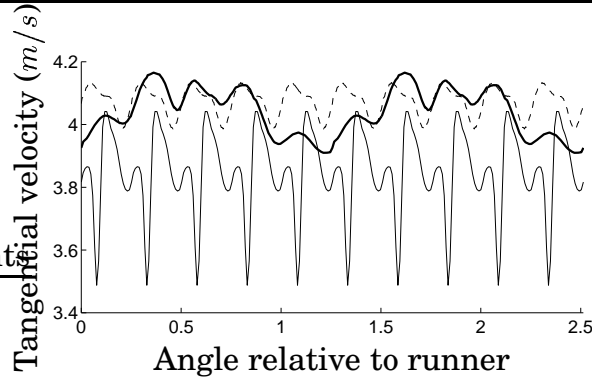
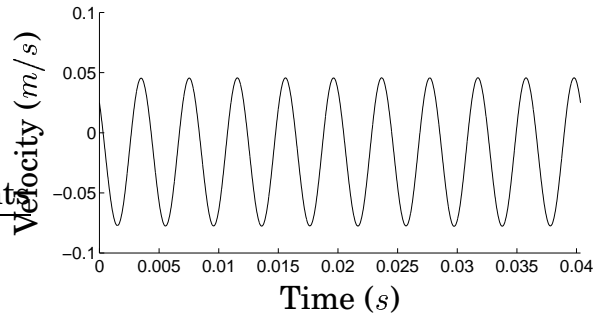


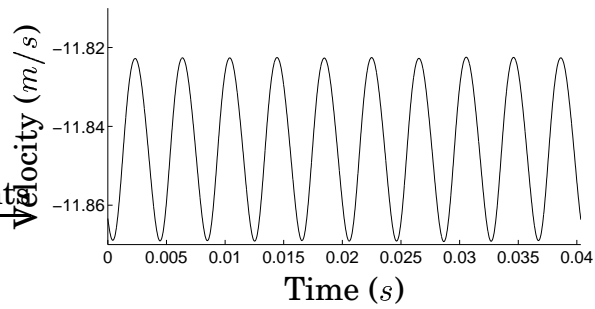
Figure 4.2: Instantaneous plot of the tangential distribution of the absolute tangential velocity at 5% of the channel width from the shroud (at radius $r = r_{max} - 0.05(r_{max} - r_{min})$). Thin curve: runner inlet; thick curve: half way between the inlet and the runner blade tip, from the runner computation; dashed curve: half way between the inlet and the runner blade tip, from the guide vane computation. The angle is in radians relative to the runner and increases in the runner rotational direction. Note that the curves have separate angle origins. Two periodic runner blade passages ($2 \cdot 2\pi/5$) and the corresponding ten guide vane passages are shown.

The time variation at the leading edge of the runner blade tip is important for capturing the time variation of the tip vortex. Figure 4.3 shows the velocity components relative to the rotating coordinate system close to the tip vortex core at mid-span of a runner blade. All components show a sinusoidal time variation with a periodicity corresponding to the number of guide vanes. The magnitudes of the fluctuations are however too small in comparison with experimental observations of cavitating tip vortices [7].

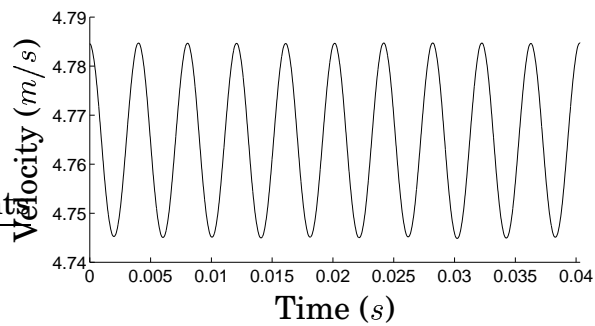
The fact that there is no frequency other than that of the guide vane wake passage shows that the method does not allow resolved turbulent fluctuations to be generated from flow instabilities in boundary layers and separation regions. An unsteady computation with an axisymmetric inlet boundary condition, which is not shown in this work, also showed this while converging to a steady result. The reason that no resolved turbulent fluctuations are generated is that both the $k - \omega$ turbulence modelling, the Van Leer upwind spatial discretization and the implicit time discretization are too stable. A less stable configuration would however not converge at all in the present case.



(a) Radial velocity.



(b) Tangential velocity.



(c) Axial velocity.

Figure 4.3: Instantaneous velocity components relative to the rotating coordinate system at the center of the tip vortex mid-span between the leading and trailing edges. The time span ($t = 0s$ to $t = 0.04s$) corresponds to a runner rotation of $2 \cdot 2\pi/5$ radians, which includes ten guide vane passages.

4.3 Discussion

It is shown in this chapter that the runner URANS computational result gives an unsteady solution, but it is only weakly unsteady. The reason for this is believed to originate in insufficiently resolved guide vane wakes and too much numerical and turbulent diffusion, which has also been observed at the runner blade wakes. Since the guide vane wakes are moving relative to the runner coordinate system, the wakes must be resolved everywhere, which is impossible with the available computational power. In large parts of the domain the flow goes diagonally through the computational control volumes, which introduces numerical diffusion that smears out the wakes too much. The flow that reaches the runner blades is more or less sinusoidal, with too small an amplitude. The gradients are thus not sharp enough to produce flow instabilities with the present stable Van-Leer upwind discretization scheme.

Another reason for the lack of unsteady effects in the tip vortex is that the leakage vortices caused by leakage flow from the pressure side to the suction side at the guide vane overhang are not included in the distributor computations. Grekula [7] shows that vortex interaction is a major source of waviness in vortex core shapes, which suggests that the guide vane overhang leakage flow is important with respect to the dynamics of the tip vortex.

The unsteady behavior of the tip vortex might also be enhanced by cavitation dynamics, since it is more or less always observed in cavitating conditions. The present computation does however not include cavitation.

Chapter 5

Conclusion

The thesis reports investigations of the turbulent flow in water turbines. The water flow in a wicket gate, in two Kaplan runners and in a Francis runner is investigated. The method of investigation is principally numerical although experimental observations and measurements, made both in the present work and by others, are incorporated in the investigations. The numerical results are qualitatively similar to both the experimental observations and measurements. The discrepancies are shown to originate both in insufficient resolution of the computations (grid quality/density/distribution, discretization order), necessary assumptions made in the computations (steady, periodic) and in problems with the measurements (inadequate measurement techniques, determination of operating condition). The comparisons show that the numerical method is reliable for computations of the flow in water turbines but that it requires that careful attention be paid to grid quality, grid density, grid distribution and discretization scheme in order to capture the details of the flow. The work particularly shows that it is difficult to preserve the thin wakes after the guide vanes and runner blades. To capture the effect of the guide vane wakes the entire flow domain must have sufficiently small control volumes to preserve the wakes, which requires an extremely large grid. The preliminary unsteady computations of the interaction between the guide vane wakes and the flow in the runner show that the present resolution must be significantly increased. The sharp gradients of the guide vane wakes are smeared out as the flow passes the insufficiently resolved computational domain. The flow that reaches the runner is more or less sinusoidal in time with too small an amplitude, and the unsteady effects are thus small. To produce good unsteady results a numerical method that better preserves the guide vane wakes must be developed

or the grid size must be significantly increased. The preservation of thin wakes in coarse grids and in flow that goes diagonally through the control volumes needs further study.

Investigations of the computational results can be used to understand the details of the flow in water turbine runners. Numerous features that occur in water turbine runner flow are captured by the present computational results. It is however difficult to extract and investigate the interesting flow features from the large amount of computational results. The present work focuses on the Kaplan tip vortex, which has shown itself to be difficult to investigate when it is small or weak. The present work uses a number of different visualization techniques to investigate the flow features. Surface restricted streamlines (smearlines) reveal important information on the flow close to surfaces. When interesting flow features have been located by the smearlines they can also be visualized with other methods, such as ordinary streamlines, to get a better understanding of the flow. The problem is however to find new interesting and important flow features that are captured by the computations. In work that is not presented in this thesis the use of feature based visualization for vortex core extraction [14] and Immersed Virtual Reality visualization has been investigated. The topics of visualization and flow feature extraction need further investigation, however.

The parallel multiblock finite volume CALC-PMB CFD code that was developed in the present work produces accurate predictions of the flow in water turbines. The parallel multiblock implementation made it possible to resolve the complicated geometries of water turbines and distributed the computational requirements over several CPUs. The gains of the use of parallel CPUs are several: the computational speed may be increased, larger problems may be solved since the memory requirement is divided between the processors, higher prediction accuracy may be achieved because of the extra memory available and parallel supercomputers or networks of workstations may be employed. The parallel efficiency of the code is excellent, with super scalar speed-up at least up to 32 processors for large 3D load balanced applications using the best configuration of computer architecture and message passing interface. However, it has been shown that the parallel efficiency may decrease drastically if the size of the problem is small, the load balancing poor or the configuration of computer architecture and message passing interface is not good. The code is also used and validated in academic test cases and in other industrial applications such as LES (Large Eddy Simulations) of the flow around vehicles and airfoils and

of heat transfer in gas turbines.

A numerical verification method based on the conservation of a subset of the angular momentum equations has been developed. The method is both a local and global error estimation method, and it may be used to show the error development along the numerical flow path. The verifications made in the present work show that the first-order hybrid discretization scheme cannot be used in computations of the flow in water turbine runners and that the second-order Van Leer discretization scheme needs improvements to give quantitatively good results. The global error of the hybrid scheme is shown to be about 30 times larger than for the Van Leer scheme. The Van Leer scheme has a global error between 0.5% and 3% for the cases computed in the present work. The present work has studied only a small part of the angular momentum balance that is important to a single vortex with known features. There are, however, several vortices of unknown features in turbomachinery flow (and most other flows as well) that must also be resolved. It is obvious that a discretization scheme that simultaneously preserves both the linear momentum equations and the general angular momentum equations is desirable.

A final conclusion that can be made from the present work is that neither the theoretical methods, the experimental methods nor the numerical methods of today are sufficient to fully describe the turbulent flow in water turbines. However, a combination of several methods gives quite a detailed picture of what is really going on in water turbine flow.

Bibliography

- [1] U. Andersson. Turbine 99 - Experiments on draft tube flow (test case T). In *Proceedings from Turbine 99 - Workshop on Draft Tube Flow*, 2000, ISSN: 1402 - 1536.
- [2] U. Andersson and R. Karlsson. Quality aspects of the Turbine 99 draft tube experiment. In *Proceedings from Turbine 99 - workshop on draft tube flow*, 2000, ISSN: 1402 - 1536.
- [3] E. Blosch, W. Shyy, and R. Smith. The role of mass conservation in pressure-based algorithms. *Numer. Heat Transfer. Part B*, 24:415–429, 1993.
- [4] S. Dahlström. Large Eddy Simulation of the Flow Around a High Lift Airfoil. Thesis for the degree of Licentiate of Engineering 00/5, Dept. of Thermo and Fluid Dynamics, Chalmers University of Technology, Gothenburg, 2000.
- [5] L. Davidson and B. Farhanieh. CALC-BFC: A Finite-Volume Code Employing Collocated Variable Arrangement and Cartesian Velocity Components for Computation of Fluid Flow and Heat Transfer in Complex Three-Dimensional Geometries. Rept. 92/4, Thermo and Fluid Dynamics, Chalmers University of Technology, Gothenburg, 1992.
- [6] J.P. Van Doormaal and G.D. Raithby. Enhancements of the SIMPLE method for predicting incompressible fluid flows. *Num. Heat Transfer*, 7:147–163, 1984.
- [7] M. Grekula. Suction side cavitation in a Kaplan turbine model runner. Internal report, ISSN 1101-0614, CHA/NAV/R-00/0070, Department of Naval Architecture and Ocean Engineering, Chalmers University of Technology, 2000.

- [8] P. Johansson and L. Davidson. Modified collocated SIMPLEC algorithm applied to buoyancy-affected turbulent flow using a multigrid solution procedure. *Num. Heat Transfer, Part B*, 28:39–57, 1995.
- [9] S. Krajnović. Large Eddy Simulations for Computing the Flow Around Vehicles. Thesis for the degree of Doctor of Philosophy, Dept. of Thermo and Fluid Dynamics, Chalmers University of Technology, Gothenburg, 2002.
- [10] P.K. Kundu. *Fluid Mechanics*. Academic Press, San Diego, California, 1990.
- [11] B. Lakshminarayana. *Fluid Dynamics and Heat Transfer of Turbomachinery*. John Wiley & Sons, Inc., New York, 1996.
- [12] M.A. Leschziner. Blade row interference effects in axial turbomachinery stages. *Von Karman Institute for Fluid Dynamics*, 1998.
- [13] G.E. Mase. *Continuum Mechanics*. McGraw-Hill, New York, first edition, 1970.
- [14] H. Nilsson. A Numerical Investigation of the Turbulent Flow in a Kaplan Water Turbine Runner. Thesis for the degree of Licentiate of Engineering 99/5, Dept. of Thermo and Fluid Dynamics, Chalmers University of Technology, Gothenburg, 1999.
- [15] H. Nilsson, U. Andersson, and S. Videhult. An experimental investigation of the flow in the spiral casing and distributor of the Hölleforsen Kaplan turbine model. Int.rep. 01/05, Dept. of Thermo and Fluid Dynamics, Chalmers University of Technology, Gothenburg, 2001.
- [16] H. Nilsson and L. Davidson. A numerical investigation of tip clearance flow in Kaplan water turbines. In *Hydro Power into the Next Century - III*, pages 327–336, 1999.
- [17] H. Nilsson and L. Davidson. A numerical investigation of the flow in the wicket gate and runner of the Hölleforsen (Turbine 99) Kaplan turbine model. To be published. In *Proceedings from Turbine 99 II*, 2001.

BIBLIOGRAPHY

- [18] S.V. Patankar. *Numerical Heat Transfer and Fluid Flow*. McGraw-Hill, New York, 1980.
- [19] W. H. Press, S. A. Teukolsky, W. T. Vetterling, and B. P. Flannery. *Numerical Recipes in FORTRAN*. CAMBRIDGE UNIVERSITY PRESS, Cambridge, second edition, 1995.
- [20] A. Sveningsson. Private communication. *Dept. of Thermo and Fluid Dynamics, Chalmers University of Technology*, 2002.
- [21] B. van Leer. Towards the ultimate conservative difference scheme. Monotonicity and conservation combined in a second order scheme. *Journal of Computational Physics*, 14:361–370, 1974.
- [22] H.K. Versteeg and W. Malalasekera. *An introduction to Computational Fluid Dynamics The Finite Volume Method*. Addison Wesley Longman Limited, Essex, England, 1995.
- [23] D.C. Wilcox. Reassessment of the scale-determining equation for advanced turbulence models. *AIAA J.*, 26(11):1299–1310, 1988.

Appendix A

Governing equations

This appendix describes the governing equations for turbulent flow in a rotating coordinate system. Appendix A.1 presents the continuity and momentum equations that fully describe the flow. Appendix A.2 presents the turbulence closure model used in the present work.

A.1 Continuity and momentum equations

From mass conservation, the continuity equation reads

$$\frac{\partial \rho}{\partial t} + \frac{\partial \rho u_i}{\partial x_i} = 0 \quad (\text{A.1})$$

Starting with Newton's second law, stating that the rate of change of momentum of a fluid particle equals the sum of the forces acting on the particle, the Navier Stokes equations (linear momentum) for incompressible flow in a rotating frame of reference read [10]

$$\begin{aligned} \frac{\partial \rho u_i}{\partial t} + \frac{\partial \rho u_i u_j}{\partial x_j} = & \\ \rho g_i - \frac{\partial p}{\partial x_i} + \frac{\partial}{\partial x_j} \left[\mu \left(\frac{\partial u_i}{\partial x_j} + \frac{\partial u_j}{\partial x_i} \right) \right] & \\ - \rho \epsilon_{ijk} \epsilon_{klm} \Omega_j \Omega_l x_m - 2\rho \epsilon_{ijk} \Omega_j u_k & \end{aligned} \quad (\text{A.2})$$

where $-\epsilon_{ijk} \epsilon_{klm} \Omega_j \Omega_l x_m$ is the centripetal term and $-2\epsilon_{ijk} \Omega_j u_k$ is the Coriolis term. The cross-diffusion term, $\frac{\partial}{\partial x_j} \left[\mu \frac{\partial u_j}{\partial x_i} \right]$, vanishes since the viscosity, μ , is constant. It is however kept in the remainder of this appendix to show its relation with the turbulence model.

Because of the potential nature of the pressure, gravitational and centripetal terms, they are put together in what is often referred to as a *reduced* pressure gradient

$$-\frac{\partial p^*}{\partial x_i} = -\frac{\partial p}{\partial x_i} + \rho g_i - \rho \epsilon_{ijk} \epsilon_{klm} \Omega_j \Omega_l x_m$$

Thus, a relation for the *reduced* pressure is

$$p^* = p - \rho g_i x_i + \rho \epsilon_{ijk} \epsilon_{klm} \Omega_j \Omega_l x_m x_i$$

In post-processing, the variation of the gravity term is assumed to be negligible and the centripetal term is simply subtracted from the *reduced* pressure to get the static pressure.

A.2 Turbulence modelling

The common way to treat turbulent flow is to decompose it into a mean and a fluctuating part (Reynolds decomposition)

$$\begin{aligned} u_i &= U_i + u'_i \\ p &= P + p' \end{aligned}$$

Inserting the Reynolds decomposition into equations A.1 and A.2 and taking the time average yields the Reynolds time averaged continuity and Navier Stokes equations in a rotating frame of reference

$$\begin{aligned} \frac{\partial \rho}{\partial t} + \frac{\partial \rho U_i}{\partial x_i} &= 0 \\ \frac{\partial \rho U_i}{\partial t} + \frac{\partial \rho U_i U_j}{\partial x_j} &= \\ -\frac{\partial P}{\partial x_i} + \frac{\partial}{\partial x_j} \left(\mu \left(\frac{\partial U_i}{\partial x_j} + \frac{\partial U_j}{\partial x_i} \right) - \overline{\rho u'_i u'_j} \right) + \rho g_i & \\ -\rho \epsilon_{ijk} \epsilon_{klm} \Omega_j \Omega_l x_m - 2\rho \epsilon_{ijk} \Omega_j U_k & \end{aligned}$$

The Reynolds stress tensor, $\overline{u'_i u'_j}$, now appearing in the Reynolds time averaged Navier Stokes equations represents correlations between the fluctuating velocities (turbulence). This tensor is unknown and must be modeled in order to close the equation system. There are several approaches to modeling the Reynolds stress tensor, such as algebraic models, one-equation models, two-equation models and Reynolds

Appendix A: Governing equations

stress models, ordered according to complexity, accuracy and computational cost. Since two-equation models are the most commonly used turbulence models today in practical applications, they will be further described.

Two-equation turbulence models fall into the class of eddy-viscosity models, which relate the Reynolds stress tensor to the velocity gradients and a turbulent viscosity. This relation is called the Boussinesq assumption, which assumes that turbulent diffusion is similar to molecular diffusion according to

$$\frac{\partial}{\partial x_j} \left(\mu \left(\frac{\partial U_i}{\partial x_j} + \frac{\partial U_j}{\partial x_i} \right) - \overline{\rho u'_i u'_j} \right) = \frac{\partial}{\partial x_j} \left((\mu + \mu_t) \left(\frac{\partial U_i}{\partial x_j} + \frac{\partial U_j}{\partial x_i} \right) \right)$$

Identification of terms yields

$$\overline{\rho u'_i u'_j} = -\mu_t \left(\frac{\partial U_i}{\partial x_j} + \frac{\partial U_j}{\partial x_i} \right)$$

However, in order to make this equation valid upon contraction (index $i = j$) together with the continuity equation, a term must be added as

$$\overline{\rho u'_i u'_j} = -\mu_t \left(\frac{\partial U_i}{\partial x_j} + \frac{\partial U_j}{\partial x_i} \right) + \frac{2}{3} \delta_{ij} \rho k$$

where $k = \frac{1}{2} \overline{u'_i u'_i}$ is the turbulent kinetic energy. The exact equation for the turbulent kinetic energy may be derived by subtracting the Reynolds averaged equations from the Navier Stokes equations, multiplying by $u_i/2$ and time averaging, yielding

$$\begin{aligned} \frac{\partial \rho k}{\partial t} + \frac{\partial \rho U_j k}{\partial x_j} = \\ - \overline{\rho u'_i u'_j} \frac{\partial U_i}{\partial x_j} - \frac{\partial}{\partial x_j} \left(\overline{u'_j p'} + \frac{1}{2} \overline{\rho u'_j u'_i u'_i} - \mu \frac{\partial k}{\partial x_j} \right) - \mu \frac{\partial u'_i}{\partial x_j} \frac{\partial u'_i}{\partial x_j} \end{aligned}$$

The terms in this equation (from left to right) are: rate of change of turbulent kinetic energy, convection, production, diffusion (by pressure velocity fluctuations, velocity fluctuations and viscosity) and dissipation, respectively. No effect of rotation appears since the rotational terms in the exact Reynolds stress transport equations in a rotating frame of reference disappear upon contraction [12]. This exact equation for the turbulent kinetic energy cannot be solved, since the stress tensor ($\overline{u'_i u'_j}$), the triple correlations ($\overline{\rho u'_j u'_i u'_i}$), the pressure diffusion ($\overline{u'_j p'}$) and

the dissipation ($\overline{\mu \frac{\partial u'_i}{\partial x_j} \frac{\partial u'_i}{\partial x_j}}$) are unknown. A modeled equation for the turbulent kinetic energy is defined as

$$\frac{\partial \rho k}{\partial t} + \frac{\partial \rho U_j k}{\partial x_j} = \frac{\partial}{\partial x_j} \left(\left(\mu + \frac{\mu_t}{\sigma_k} \right) \frac{\partial k}{\partial x_j} \right) + P_k - \rho \varepsilon$$

where the production term is obtained from the production term in the exact equation for the turbulent kinetic energy together with the Boussinesq assumption, yielding

$$P_k = \mu_t \left(\frac{\partial U_i}{\partial x_j} + \frac{\partial U_j}{\partial x_i} \right) \frac{\partial U_i}{\partial x_j}$$

The turbulent dissipation, ε [m^2/s^3], can be determined by an additional transport equation. In the present work the turbulent dissipation is computed in terms of specific dissipation, ω [$1/s$]. The new turbulent quantity introduced is computed by an equation similar to the modeled equation for turbulent kinetic energy, since the exact equation is too complex. Dimensional reasoning yields the ω equation as

$$\frac{\partial \rho \omega}{\partial t} + \frac{\partial \rho U_j \omega}{\partial x_j} = \frac{\partial}{\partial x_j} \left[\left(\mu + \frac{\mu_t}{\sigma_\omega} \right) \frac{\partial \omega}{\partial x_j} \right] + \frac{\omega}{k} (c_{\omega 1} P_k - c_{\omega 2} \rho k \omega)$$

where the turbulent viscosity, μ_t , is defined as

$$\mu_t = \rho \frac{k}{\omega}$$

the turbulent dissipation reads

$$\varepsilon = \beta^* \omega k$$

and the closure coefficients are

$$\beta^* = 0.09, c_{\omega 1} = \frac{5}{9}, c_{\omega 2} = \frac{3}{40}, \sigma_k = 2 \text{ and } \sigma_\omega = 2$$

The two-equation model described above is the $k - \omega$ model by Wilcox [23]. The main advantage of this model is that it gives good results throughout the boundary layer without complicated correction functions on the basis of distance to the wall. It is a simple turbulence model that enhances computational stability.

A.3 Summary of the solved equations

The equations that are solved in the present work are the continuity equation

$$\frac{\partial \rho U_i}{\partial x_i} = 0$$

the linear momentum equations

$$\frac{\partial \rho U_i}{\partial t} + \frac{\partial \rho U_i U_j}{\partial x_j} = -\frac{\partial P^*}{\partial x_i} + \frac{\partial}{\partial x_j} \left((\mu + \mu_t) \frac{\partial U_i}{\partial x_j} \right) - 2\rho \epsilon_{ijk} \Omega_j U_k$$

the turbulent kinetic energy equation

$$\frac{\partial \rho k}{\partial t} + \frac{\partial \rho U_j k}{\partial x_j} = \frac{\partial}{\partial x_j} \left(\left(\mu + \frac{\mu_t}{\sigma_k} \right) \frac{\partial k}{\partial x_j} \right) + P_k - \rho \varepsilon$$

and the specific dissipation equation

$$\frac{\partial \rho \omega}{\partial t} + \frac{\partial \rho U_j \omega}{\partial x_j} = \frac{\partial}{\partial x_j} \left[\left(\mu + \frac{\mu_t}{\sigma_\omega} \right) \frac{\partial \omega}{\partial x_j} \right] + \frac{\omega}{k} (c_{\omega 1} P_k - c_{\omega 2} \rho k \omega)$$

The *reduced* pressure is defined as

$$P^* = P - \rho g_i x_i + \rho \epsilon_{ijk} \epsilon_{klm} \Omega_j \Omega_l x_m x_i$$

The turbulent viscosity is defined as

$$\mu_t = \rho \frac{k}{\omega}$$

The turbulence production reads

$$P_k = \mu_t \left(\frac{\partial U_i}{\partial x_j} + \frac{\partial U_j}{\partial x_i} \right) \frac{\partial U_i}{\partial x_j}$$

The turbulent dissipation reads

$$\varepsilon = \beta^* \omega k$$

The closure coefficients are

$$\beta^* = 0.09, c_{\omega 1} = \frac{5}{9}, c_{\omega 2} = \frac{3}{40}, \sigma_k = 2 \text{ and } \sigma_\omega = 2$$

Appendix B

The code

A parallel multiblock finite volume code, CALC-PMB (Parallel Multi-Block), for computations of the turbulent flow in complex geometries was developed. The main features of the code are the use of conformal block structured boundary fitted coordinates, a pressure correction scheme (SIMPLEC, appendix B.3.1), Cartesian velocity components as principal unknowns and collocated grid arrangement together with Rhie and Chow interpolation (appendix B.3.2). The governing equations (appendix A) of fluid flow in a rotating coordinate system are discretized using a finite volume method (appendix B.1). The turbulence is modeled using a low-Reynolds $k - \omega$ turbulence model (appendix A). For grid generation, an interface to the commercial grid generator ICEM CFD/CAE was implemented. In the parallel multiblock algorithm, two ghost cell planes are employed at the block interfaces (Appendix B.7). The message passing at the interfaces is done using either PVM (Parallel Virtual Machine) or MPI (Message Passing Interface). The code may be run in parallel on everything from heterogeneous networks of workstations to Linux clusters and distributed and shared memory supercomputers. The gains of the parallel implementation are several: the computational speed may be increased, larger problems may be solved since the memory requirement is divided between the processors and more exact solutions may be obtained because of the extra memory available.

B.1 The finite volume method

When using a finite volume method [5, 18], the computational domain is divided into a finite number of control volumes (see fig. B.1). In order

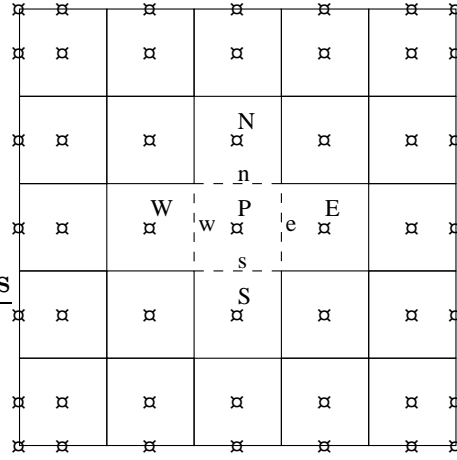


Figure B.1: The division of the domain into a finite number of control volumes. Two-dimensional example. The nodes are placed in the center of the control volumes except at the boundaries, where they are placed at the boundary. At the center control volume (dashed line), the nomenclatures for control volumes (nodes (P, E, W, N, S) and faces (e, w, n, s)) are introduced.

to deal with complex geometries, a boundary fitted coordinate method, where the control volumes are allowed to be mildly skewed to fit the boundaries, is used.

The transport equation for a general dependent scalar variable, Φ , in Cartesian coordinates can be written as

$$\frac{\partial}{\partial t} (\rho\Phi) + \frac{\partial}{\partial x_i} \left(\rho u_i \Phi - \Gamma_\Phi \frac{\partial \Phi}{\partial x_i} \right) = S_\Phi \quad (\text{B.1})$$

Defining the total flux (convective and diffusive) as

$$I_i = \rho u_i \Phi - \Gamma_\Phi \frac{\partial \Phi}{\partial x_i} \quad (\text{B.2})$$

equation B.1 can be rewritten as

$$\frac{\partial}{\partial t} (\rho\Phi) + \frac{\partial I_i}{\partial x_i} = S_\Phi \quad (\text{B.3})$$

Equation B.3 is integrated over a control volume and a time step yielding

$$\int_{\Delta t} \int_{CV} \frac{\partial}{\partial t} \rho\Phi dV dt + \int_{\Delta t} \int_{CS} I_i dA_i dt = \int_{\Delta t} \int_{CV} S_\Phi dV dt \quad (\text{B.4})$$

where Gauss' divergence theorem

$$\int_{CV} \frac{\partial I_i}{\partial x_i} dV = \int_{CS} I_i dA_i$$

has been used to convert the total flux control volume integral to a control surface integral.

If the control volumes are non-deformable, the order of integration can be changed in the rate of change term in equation B.4. Assuming that ρ is constant over both time and space and that Φ is constant over the control volume, we get

$$\int_{CV} \int_{\Delta t} \frac{\partial}{\partial t} \rho \Phi dt dV = \rho (\Phi_P - \Phi_P^o) \Delta V$$

using a first-order backward differencing scheme.

The volume integrals of the total flux and source terms in equation B.4 are performed assuming a spatially constant source term, S , over the control volume and a spatially constant flux over the control volume faces, yielding

$$\rho (\Phi_P - \Phi_P^o) \Delta V + \int_{\Delta t} \sum_{face=e,w,n,s,h,l} (I_i A_i)_{face} dt = \int_{\Delta t} S \Delta V dt$$

where e , w , n , s , h and l refer to the faces of the control volume.

The remaining time integrals may be evaluated by assuming that the integrands are constant or varying linearly in time over Δt . The value of the integrand can be obtained from the previous time step, from the present time step or from a combination of both according to

$$\int_{\Delta t} S \Delta V dt = [\theta S + (1 - \theta) S^o] \Delta V \Delta t$$

and in a similar way for the total flux term.

The weighting parameter, θ , goes from 0 to 1 and determines how much of the present value should be used and how much of the old value should be used. If $\theta = 0$, it is an explicit scheme, which uses only old values. If $\theta = 1$, it is a fully implicit scheme, which uses only present values. If $\theta = 0.5$, it is a Crank-Nicolson scheme, which uses an equal amount of both old and present values. Explicit and fully implicit schemes are first-order accurate in time and the Crank-Nicolson scheme is second-order accurate in time.

The discretized equation is rearranged, using a spatial discretization scheme for I_i , to the standard form

$$\begin{aligned}
 a_P \Phi_P &= \sum_{NB} a_{NB} [\theta \Phi_{NB} + (1 - \theta) \Phi_{NB}^o] \\
 &+ \left[a_P^o - \sum_{NB} (1 - \theta) a_{NB} \right] \Phi_P^o \\
 &+ \theta S_u + (1 - \theta) S_u^o
 \end{aligned} \tag{B.5}$$

where the coefficient of the central node is

$$a_P = \theta \sum_{NB} a_{NB} - S_P + a_P^o$$

The central coefficient at the previous time step is

$$a_P^o = \rho \frac{\Delta V}{\Delta t}$$

and the source term has been linearized as

$$[\theta S + (1 - \theta) S^o] \Delta V = \theta S_u + (1 - \theta) S_u^o + S_P \Phi_P$$

where S_P is chosen always to be negative, which gives a diagonally dominant coefficient matrix and numerical stability. During the computations the contribution from the previous time step in equation B.5 is applied as a source term.

When computing the steady transport equation, $\theta = 1$ and $a_P^o = 0$ is used, yielding

$$a_P \Phi_P = \sum_{NB} a_{NB} \Phi_{NB} + S_u$$

where the central coefficient is

$$a_P = \sum_{NB} a_{NB} - S_P$$

and the source term has been linearized as

$$S \Delta V = S_u + S_P \Phi_P$$

The coefficients of the neighboring nodes, a_{NB} , depend on which spatial discretization scheme is used (appendix B.2). The spatial discretization scheme is evaluated using the most recent convections and diffusions. Solving equation system B.5 with known or simultaneously computed velocity and source fields gives an approximate solution to the unsteady transport equation.

B.2 Spatial discretization schemes

To solve the discretized transport equation, B.5, the total fluxes (equation B.2) through the faces of the control volume must be known. Since all variables are calculated at the nodes, some kind of interpolation must be used to get the fluxes through the control volume faces. A number of ways of doing this are described in the literature. Some of the discretization schemes included in the code are described in the following sections. All schemes are presented for the east face (e) but the rest of the faces have similar expressions.

B.2.1 The central scheme

The central scheme approximates the face values as

$$\Phi_e = (1 - f_e) \Phi_P + f_e \Phi_E$$

where f_e is an interpolation factor, allowing non-uniform grids, defined as

$$\begin{aligned} f_e &= \frac{\delta r_{Pe}}{\delta r_{PE}} \\ \delta r_{Pe} &= |\vec{r}_e - \vec{r}_P| \\ \delta r_{PE} &= |\vec{r}_E - \vec{r}_P| \end{aligned}$$

where \vec{r} is the position vector pointing at nodes or the center of the control volume faces, denoted according to figure B.1. For uniform grids, $f_e = 0.5$. The diffusion is also discretized using central differencing. Two major drawbacks of the central scheme are that it is unbounded, which can lead to unphysical oscillations and numerical problems, and that it is unable to identify flow direction. In a strongly convective flow, the face values should be influenced more by the upstream node than by the downstream node.

B.2.2 The first-order upwind scheme

In the first-order upwind scheme, the face values are set equal to the upwind (or upstream) node as

$$\begin{aligned} \Phi_e &= \Phi_P \quad \text{for } U_e > 0 \\ \Phi_e &= \Phi_E \quad \text{for } U_e < 0 \end{aligned}$$

The diffusion is discretized using central differencing. The major drawback of the first-order upwind scheme is that it is first-order accurate.

B.2.3 The hybrid scheme

This scheme is a combination of the central and the first-order upwind schemes. It uses the central scheme if the magnitude of the Peclet number is below two and the first-order upwind scheme otherwise.

$$\begin{aligned} \Phi_e &= \Phi_P && \text{for } U_e > 0 \text{ and } |P_{e_e}| \geq 2 \\ \Phi_e &= \Phi_E && \text{for } U_e < 0 \text{ and } |P_{e_e}| \geq 2 \\ \Phi_e &= f_x \Phi_E + (1 - f_x) \Phi_P && \text{for } |P_{e_e}| < 2 \end{aligned}$$

The Peclet number reads

$$P_{e_e} = \frac{F_e}{D_e}$$

where F_e is the convective mass flux per unit area and D_e is the diffusion conductance at cell faces. The diffusion is discretized using central differencing for $|P_{e_e}| < 2$ and is otherwise neglected. The hybrid scheme thus uses the first-order upwind scheme if convection is dominant and the central scheme if diffusion is not negligible. The major drawback of the hybrid scheme is that convection is dominant in most flows and the hybrid scheme can be regarded as a first-order upwind scheme.

B.2.4 The Van Leer Scheme

This scheme of Van Leer [21] is of second-order accuracy except at local minima or maxima, where its accuracy is of the first order. One advantage of this scheme is that it is bounded. For east face it can be written

$$\begin{aligned} \Phi_e &= \Phi_P && \text{if } |\Phi_E - 2\Phi_P + \Phi_W| \geq |\Phi_E - \Phi_W| \\ \Phi_e &= \Phi_P + \frac{(\Phi_E - \Phi_P)(\Phi_P - \Phi_W)}{\Phi_E - \Phi_W} && \text{otherwise} \end{aligned}$$

if $U_e > 0$ and

$$\begin{aligned} \Phi_e &= \Phi_E && \text{if } |\Phi_P - 2\Phi_E + \Phi_{EE}| \geq |\Phi_P - \Phi_{EE}| \\ \Phi_e &= \Phi_E + \frac{(\Phi_P - \Phi_E)(\Phi_E - \Phi_{EE})}{\Phi_P - \Phi_{EE}} && \text{otherwise} \end{aligned}$$

if $U_e < 0$. The diffusion is discretized using central differencing.

The Van Leer scheme is thus a first-order upwind scheme with a correction term, which gives it second-order accuracy.

B.3 Pressure-velocity coupling

The Reynolds averaged Navier Stokes equations for incompressible flow depend on the pressure distribution, which must be solved together with the velocities. Since there is no equation for the pressure for incompressible flow, some kind of pressure-velocity coupling is needed. The pressure-velocity coupling used in this code is called SIMPLEC and is described in the following section.

B.3.1 The SIMPLEC method

The SIMPLEC [6] method (Semi-Implicit Method for Pressure-Linked Equations, Consistent) supplying the pressure-velocity coupling, is used to solve the Reynolds averaged Navier Stokes and continuity equations. The method has its origins in staggered grid methodology and is adapted to collocated grid methodology through the use of Rhie & Chow interpolation, described in the next section. The nomenclature used to derive the expressions in this section is upper case index letters, E, W, N, S, H, L , for non-staggered (scalar) control volumes and lower case index letters, e, w, n, s, h, l , for staggered (velocity) control volumes, i.e. on the scalar control volume faces (see fig. B.1). The derivations are made only on the e staggered control volume, but the other directions are treated in a similar way.

Defining pressure and velocity corrections, p' and u'_i , as the difference between the pressure and velocity field, p and u_i , at the current iteration (*new*) and the pressure and velocity field, p^* and u_i^* , from the previous iteration (*old*), we have

$$\begin{aligned} p &= p^* + p' \\ u_i &= u_i^* + u'_i \end{aligned} \tag{B.6}$$

The discretized momentum equations for the *old* velocities and pressure in a staggered control volume

$$a_e^u u_{i_e}^* = \sum a_{nb}^u u_{i_{nb}}^* + (p_P^* - p_E^*) A_{i_e} + b_{u_{i_e}}$$

are subtracted from the discretized momentum equations for their *new* values

$$a_e^u u_{i_e} = \sum a_{nb}^u u_{i_{nb}} + (p_P - p_E) A_{i_e} + b_{u_{i_e}}$$

yielding

$$a_e^u u'_{i_e} = \sum a_{nb}^u u'_{i_{nb}} + (p'_P - p'_E) A_{i_e} \tag{B.7}$$

The omission of the term $\sum a_{nb}^u u'_{nb}$ is the main approximation of the SIMPLE [18] algorithm, giving

$$u'_{ie} = (p'_P - p'_E) \frac{A_{ie}}{a_e^u}$$

This omission will have no impact on the final solution, since $u'_{nb} = 0$ for a converged solution. However, this omission is rather inconsistent since the term on the left-hand side of equation B.7 is of the same order as those omitted. A more consistent approach is obtained by subtracting the term $\sum a_{nb}^u u'_{ie}$ from both sides of eq. B.7. This yields

$$\left(a_e^u - \sum a_{nb}^u\right) u'_{ie} = \sum a_{nb}^u (u'_{inb} - u'_{ie}) + (p'_P - p'_E) A_{ie}$$

The omission of the term $\sum a_{nb}^u (u'_{inb} - u'_{ie})$ is the consistent approximation of the SIMPLER algorithm, giving

$$u'_{ie} = \frac{A_{ie}}{a_e^u - \sum a_{nb}^u} (p'_P - p'_E)$$

where $a_e^u = a_e^{u'}/\alpha$, where $a_e^{u'} = \sum a_{nb}^u$ and α is the velocity underrelaxation. Finally, we get an expression for the *new* face velocities from eq. B.6 as

$$u_{ie} = u_{ie}^* + d_e (p'_P - p'_E) \tag{B.8}$$

where

$$d_e = \frac{A_{ie}}{a_e^u - \sum a_{nb}^u}$$

and, by analogy,

$$\begin{aligned} u_{iw} &= u_{iw}^* - d_w (p'_P - p'_W) \\ u_{in} &= u_{in}^* + d_n (p'_P - p'_N) \\ u_{is} &= u_{is}^* - d_s (p'_P - p'_S) \\ u_{ih} &= u_{ih}^* + d_h (p'_P - p'_H) \\ u_{il} &= u_{il}^* - d_l (p'_P - p'_L) \end{aligned} \tag{B.9}$$

The continuity equation in unsteady flow is given by

$$\frac{\partial \rho}{\partial t} + \frac{\partial \rho u_i}{\partial x_i} = 0$$

In this work the incompressible flow without buoyancy effects is computed, which means that ρ is constant and the time term vanishes. Inserting these corrected velocities into the discretized continuity equation of a non-staggered control volume

$$\sum_{C.S.} (\rho u_{i_{nb}} A_{i_{nb}}) = 0$$

and identifying coefficients gives a discretized equation for the pressure correction

$$a_P p'_P = a_E p'_E + a_W p'_W + a_N p'_N + a_S p'_S + a_H p'_H + a_L p'_L + b_{p'_P} \quad (\text{B.10})$$

where

$$\begin{aligned} a_P &= a_E + a_W + a_N + a_S + a_H + a_L \\ a_E &= \rho_e \frac{A_e^2}{a_e^u - \sum a_{nb}^u} \\ &\vdots \\ b_{p'_P} &= - \sum_{C.S.} (\rho u_{i_{nb}}^* A_{i_{nb}}) \end{aligned}$$

This pressure correction equation is solved using a_{nb}^u and $u_{i_{nb}}^*$ values (on the scalar control volume faces) from the momentum equations. Since this code utilises a collocated grid arrangement, the a_{nb}^u values are obtained from linear interpolation of the a_P^u values and the $u_{i_{nb}}$ values are obtained from Rhie & Chow interpolation (described in appendix B.3.2) of the u_{i_P} values. The *new* pressure field may then be obtained from eq. B.6, and the *new* convections (through the scalar control volume faces) and the node velocities are corrected according to eqs. B.8 and B.9.

B.3.2 Rhie & Chow interpolation

Since this code utilises a collocated grid arrangement, the convections through the faces needed for the pressure correction equation are obtained from Rhie & Chow interpolation, described below.

The face velocity is usually obtained by linear interpolation, i.e.

$$u_{i_e} = f_e u_{i_E} + (1 - f_e) u_{i_P}$$

where f_e is an interpolation factor, allowing non-uniform grids, defined

as

$$\begin{aligned} f_e &= \frac{\delta r_{Pe}}{\delta r_{PE}} \\ \delta r_{Pe} &= |\vec{r}_e - \vec{r}_P| \\ \delta r_{PE} &= |\vec{r}_E - \vec{r}_P| \end{aligned}$$

where \vec{r} is the position vector pointing at nodes or the center of the control volume faces, denoted according to figure B.1. In a collocated grid arrangement, however, this may lead to pressure oscillations. To avoid this, the face velocities are calculated by subtracting and adding the pressure gradient, i.e.

$$u_{ie} = f_e u_{iE} + (1 - f_e) u_{iP} - \overline{\left(-\frac{\partial p}{\partial x_i} \frac{\delta V}{a_P} \right)}_e + \left(-\frac{\partial p}{\partial x_i} \frac{\delta V}{a_P} \right)_e$$

The pressure gradient terms in this expression are calculated in different ways. The first is calculated as the mean value of the pressure gradient in the P and E nodes, i.e.

$$\begin{aligned} \overline{\left(-\frac{\partial p}{\partial x_i} \frac{\delta V}{a_P} \right)}_e &= -\frac{1}{2} \left(\left(\frac{\partial p}{\partial x_i} \right)_E + \left(\frac{\partial p}{\partial x_i} \right)_P \right) \left(\frac{\delta V}{a_P} \right)_e \\ &= -\frac{1}{2} \left(\frac{p_{EE} - p_P}{\delta x_{iPEE}} + \frac{p_E - p_W}{\delta x_{iWE}} \right) \left(\frac{\delta V}{a_P} \right)_e \end{aligned}$$

The second is calculated on the face, i.e.

$$\left(-\frac{\partial p}{\partial x_i} \frac{\delta V}{a_P} \right)_e = - \left(\frac{p_E - p_P}{\delta x_{iPE}} \right) \left(\frac{\delta V}{a_P} \right)_e$$

Equidistant grid yields $\delta x_{iPEE} = \delta x_{iWE} = 2\delta x_{iPE}$ and

$$\begin{aligned} u_{ie} &= \frac{1}{2} (u_{iE} + u_{iP}) \\ &+ \frac{1}{4\delta x_{iPE}} \left(\frac{\delta V}{a_P} \right)_e [p_{EE} - 3p_E + 3p_P - p_W] \end{aligned} \quad (\text{B.11})$$

which is used to calculate the source term in the pressure correction equation. To deal with non-equidistant grids, the first term is calculated as using linear interpolation and the second term is calculated as in equation B.11 since it is simply a fourth-order derivative term that dampens oscillations [8], yielding

$$u_{ie} = f_e u_{iE} + (1 - f_e) u_{iP} + \frac{1}{4\delta x_{iPE}} \left(\frac{\delta V}{a_P} \right)_e [p_{EE} - 3p_E + 3p_P - p_W]$$

B.4 Boundary conditions

The pressure correction, p' , has an implicit homogenous Neumann boundary condition on all boundaries [18], i.e.

$$\frac{\partial p'}{\partial n} = 0$$

where n is the coordinate direction normal to the boundary. An inhomogenous Neumann boundary condition is used to obtain the pressure at all boundaries, i.e.

$$\frac{\partial^2 P}{\partial n^2} = 0$$

where n is the coordinate direction normal to the boundary.

Boundary conditions for the velocities and other variables are described in the following sections.

B.4.1 Walls

CALC-PMB can use both wall-functions and low-Reynolds number wall treatment. All computations in the present work use a low-Reynolds number wall treatment and the low-Reynolds number $k - \omega$ turbulence model of Wilcox [23], but both methods are briefly described below.

Using a low-Reynolds number wall treatment, the sharp gradients at the walls are resolved down to the viscous sublayer at $y^+ = 1$. The term *low-Reynolds number* refers to the *local* Reynolds number, which is low in the viscous sublayer. Low-Reynolds number boundary conditions for the k and ω equations of the $k - \omega$ turbulence model of Wilcox are

$$\begin{aligned} k &= 0 \\ \omega &= \frac{6\nu}{c_{\omega 2} y^2} \end{aligned}$$

where the ω boundary condition is applied at the node closest to the wall, for $y^+ < 2.5$. The k boundary condition and the wall velocity are specified at the wall. Most of the low Reynolds number models apply correction functions to the turbulence equations to get the correct near wall behavior or to improve certain features of the results. The $k - \omega$ turbulence model of Wilcox can be integrated throughout the viscous sublayer without complicated correction functions. Wilcox proposes correction functions to account for transition and surface roughness

etc. but they are not used in the present work. Low Reynolds number models are very time consuming as a result of the large number of nodes and the slower convergence of a finer resolution.

Wall functions are derived from the log-law

$$\begin{aligned}\frac{U}{u_*} &= \frac{1}{\kappa} \ln(Ey^+) \\ \kappa &= 0.41 \\ E &= 9.0 \\ y^+ &= \frac{u_* y}{\nu}\end{aligned}$$

where the friction velocity, u_* , is iteratively determined. Wall functions assume that the flow near the walls behaves like a fully developed turbulent boundary layer. This is almost never true, but wall functions are still commonly used in order to minimize the computational effort. Using wall functions, the first node is located at a distance of $30 \leq y^+ \leq 100$ from the wall and the computed wall function value is fixed in this node. If the $k - \omega$ turbulence model and wall functions are used, k and ω are prescribed in the node closest to the wall as

$$\begin{aligned}k_{wall} &= \frac{u_*^2}{(\beta^*)^{1/2}} \\ \omega_{wall} &= \frac{u_*}{(\beta^*)^{1/2} \kappa y}\end{aligned}$$

Assuming that the wall shear stress is constant to the first node, the log-law yields a first node value for the turbulent viscosity as [5]

$$\mu_t = \frac{\rho u_* y \kappa}{\ln(Ey^+)}$$

Wall functions are less time consuming than low-Reynolds number wall treatment since the boundary layer is not resolved, but more of the physics is approximated.

B.4.2 Inlet/outlet conditions

At an inlet, all flow properties are prescribed to an approximate velocity profile. They can be interpolated from experimental data or from a fully developed profile, for instance a parabolic profile for laminar flow or a 1/7th profile for a turbulent flow.

At a large outlet, sufficiently far downstream and without area change, the flow may be assumed to be fully developed, which implies negligible streamwise gradients of all variables, i.e.

$$\frac{\partial \Phi}{\partial n} = 0$$

where n is the coordinate direction normal to the outlet.

In order to get a mathematically well posed SIMPLEC algorithm, mass flux must be globally conserved [3]. It is a necessary constraint for the pressure correction equation to be consistent. It also increases the convergence rate considerably and has positive effects on open boundaries where inflow is occurring. A velocity increment

$$u_{incr} = \frac{\dot{m}_{in} - \dot{m}_{out}^{comp}}{(\rho A)_{out}}$$

where \dot{m}_{in} is the convection into the domain at the inlet, \dot{m}_{out}^{comp} is the computed convection out of the domain at the outlet and A is the outlet area, is added to the computed velocity at the outlet, i.e.

$$u_{out} = u_{out}^{comp} + u_{incr}$$

This ensures that global continuity is fulfilled at each iteration.

B.4.3 Periodic boundaries

Periodic boundaries can be of two types: translational and rotational. These types of boundary conditions must come in pairs, one boundary connected to another. A rotational transformation of vector quantities is applied on the periodic boundaries. The periodic boundaries may then be treated as though they were connected to each other, since rotational periodicity has no impact on scalar quantities and translational periodicity has no impact on either vector or scalar quantities.

B.5 Solving the discretized equations

The discretized equations of fluid flow yields a system of linear algebraic equations that need to be solved. The code uses a TDMA (Tri-Diagonal Matrix Algorithm) solver [22]. In 3D, each node has six neighbors and at least a septa-diagonal linear system is obtained. The main idea of the TDMA is to pick a main direction and rewrite the equation system in a tri-diagonal form, where the other directions are included

in a source term. This smaller problem may be solved by Gaussian elimination, yielding a recursive algorithm that solves the small linear equation system. The convergence of the TDMA is fastest in the main direction. Each linear equation system is thus solved three times for 3D problems, with alternating main directions. The TDMA algorithm is computationally inexpensive and it has the advantage that it requires a minimum amount of storage.

B.6 Convergence criteria

An iteratively converged solution is assumed to be reached when the largest normalized residual of the momentum equations, the continuity equation and the turbulence equations is reduced to 10^{-3} [14]. The residuals of the momentum equation are normalized by the sum of the mass flow through the turbine and the mass flow through the periodic surfaces multiplied by the largest velocity component in the computational domain. The residual of the continuity equation is normalized by the sum of the mass flow through the turbine and the mass flow through the periodic surfaces. The residuals of the turbulence equations are normalized by the largest residual during the iterations.

B.7 The parallel multiblock implementation

The finite volume method, described in appendix B.1, can be used for both structured and unstructured grids and the control volumes may have all kinds of shapes. The CALC-PMB CFD code uses conformal block structured hexahedral grids that are generated in the ICEM CFD commercial grid generation software. The term *hexahedral* refers to a control volume with six faces and arbitrarily placed vertices. The term *structured* means that the control volumes are arranged as an ordered 3D matrix. The term *block structured* means that there are several blocks of structured grids that are connected to each other. The term *conformal* means that the grid lines must be continuous over block interfaces. Figure B.2 shows an example of a single block structured grid that is decomposed into four smaller structured grids, forming a multiblock topology. The effect of cyclic (or periodic) faces that attaches the left side with the right side is also shown in the figure. By overlapping the small grids two control volumes, *inner boundary conditions* can be exchanged between the blocks during the iterations. The control volu-

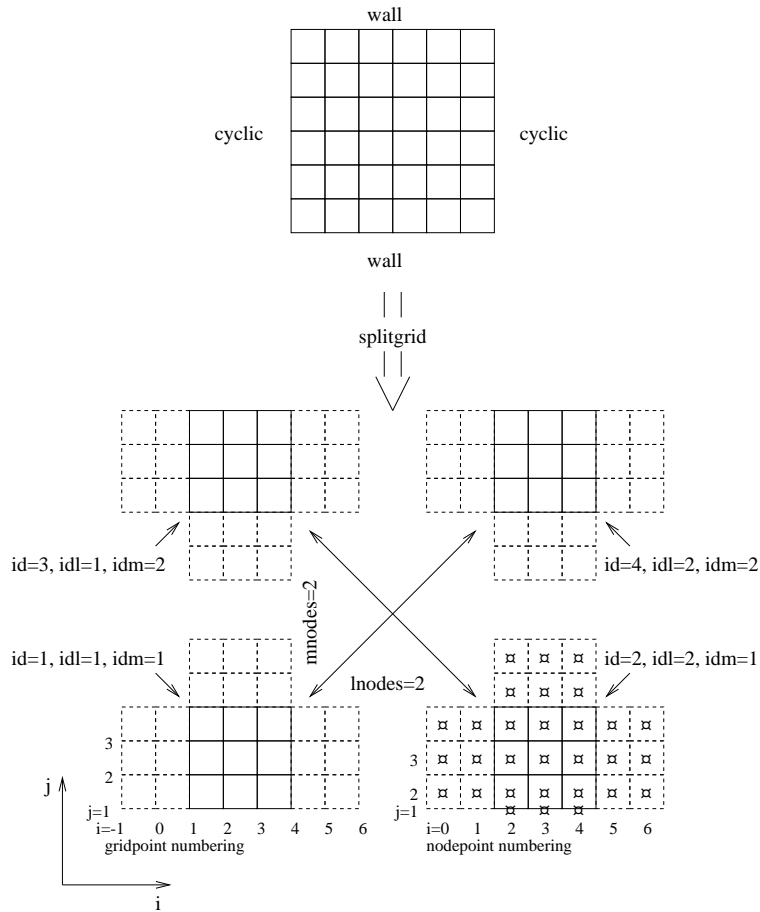


Figure B.2: The multiblock principle. The blocks have id numbers 1 to 4 and they are arranged in a matrix of $lnodes \times mnodes$ blocks. The structured decomposition also allows the blocks to be numbered in a structured way by idl and idm . The numbering of grid-points and node-points is also shown. Dashed control volumes are overlapping other control volumes.

mes close to the *inner boundaries* thus have neighbors in other blocks. The finite volume method is applied to the control volumes at *inner boundaries* exactly as though they were an interior control volume. The information in the overlapping control volumes is updated whenever it is needed (see section B.7.1). By using a message passing interface such as PVM (Parallel Virtual Machine) or MPI (Message Passing Interface) the blocks may be distributed to separate CPUs during the computations, which distributes the computational requirements and speeds up the computations (see Paper II).

Figure B.2 shows a decomposition of a single block grid that is structured and could have been computed with a single block structured solver. The multiblock principle may also be used to create an unstructured topology, which is a collection of several structured blocks where the global grid is not structured. Unstructured multiblock topologies make it possible to compute the flow in complicated geometries. Figure B.3 shows an example of the complicated unstructured multiblock topology that was used for some of the computations in the present work. The topology is periodic so that the left side can be attached to the right side during the computations. More recent multiblock topologies of the present work are simpler since the ICEM CFD commercial grid generation software has been improved.

B.7.1 Numerical procedure

The numerical procedure for a steady computation is summarized below. The velocity and pressure fields together with any other scalar field are calculated by guessing initial values of the fields and iterating through pts. I - X until convergence is reached.

I The discretized momentum equations

$$a_P u_{iP}^* = \sum a_{NB} u_{iNB}^* + (p_W^* - p_E^*) A_{iP} + b_{u_{iP}}$$

are solved.

II The inter-block boundary conditions for a_P from the discretized momentum equations are exchanged since they are needed for the Rhie & Chow interpolation.

III The convections are calculated using Rhie & Chow interpolation

$$conv_e = (\rho u_i A_i)_e + \left(\frac{A}{4a_P} \right)_e [p_{EE} - 3p_E + 3p_P - p_W]$$

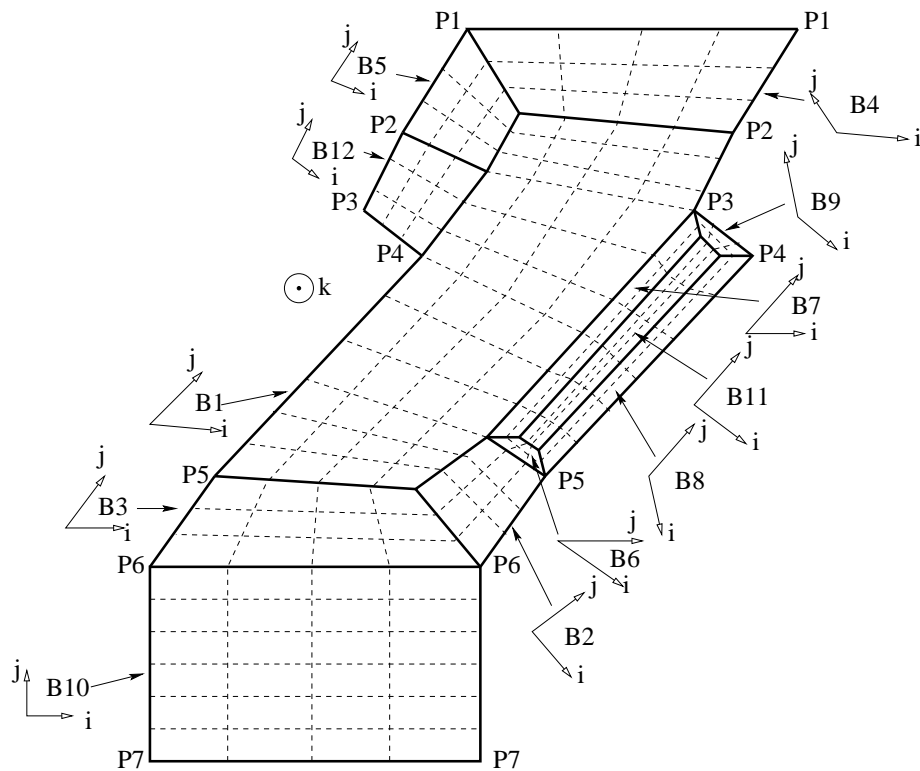


Figure B.3: A 2D view of a Kaplan runner multiblock topology. The blocks are labeled B1-B12. Some periodic grid points are labeled P1-P7. Solid lines are block boundaries. Dashed lines are examples of grid lines inside the blocks. The orientations of the blocks are shown at each block label. The k-direction is common for all blocks.

where the $(a_P)_e$ values are obtained from linear interpolation.

- IV The continuity error, needed for the source term in the pressure correction equation, is calculated from these convections.
- V The discretized pressure correction equation

$$a_P p'_P = a_E p'_E + a_W p'_W + a_N p'_N + a_S p'_S + a_H p'_H + a_L p'_L + b_{p'_P}$$

where $b_{p'_P}$ is the continuity error, is solved.

- VI The inter-block boundary conditions for the pressure correction are exchanged.
- VII The pressure, convections and velocities are corrected as

$$\begin{aligned} p_P &= p_P^* + (p'_P - p'_{P_{ref}}) \\ conv_e &= conv_e^* + \rho_e A_{ie} d_e (p'_P - p'_E) \\ u_{iP} &= u_{iP}^* + d_P (p'_W - p'_E) \end{aligned}$$

where $p'_{P_{ref}}$ is a reference value for p' from one point in the global computational domain. The velocity correction is actually not necessary, but it has proven to increase the convergence rate.

- VIII Inter-block boundary conditions for all variables are exchanged.
- IX Other discretized transport equations are solved.
- X The residual is calculated (see appendix B.6) and compared with the convergence criteria.

For unsteady computations, the discretized unsteady equations are solved similar to the steady procedure for each time step. The solution at the previous time step is then updated from the newly computed solution, the time is proceeded and the procedure is repeated for the number of time steps that need to be computed.

Appendix C

PAPERS

This appendix contains some of the papers, conference contributions and internal reports that have been produced in the present work. The papers are attached in chronological order since some of the findings in earlier are used in subsequent papers.

Paper I

A Numerical Comparison of Four Operating Conditions in a Kaplan Water Turbine, Focusing on Tip Clearance Flow.

By

Håkan Nilsson and Lars Davidson

Published in the proceedings of the
20th IAHR Symposium,
August 6-9, 2000,
Charlotte, North Carolina, U.S.A.

Paper II

Parallel Multiblock CFD Computations Applied to Industrial Cases.

By

Håkan Nilsson, Simon Dahlström
and Lars Davidson

Published in the proceedings of the conference
Parallel Computational Fluid Dynamics
- Trends and Applications,
May 22-25, 2000,
Trondheim, Norway,
Elsevier Science B.V., pp. 525–532, 2001

Paper III

A Validation of Parallel Multiblock CFD Against the GAMM Francis Water Turbine Runner at Best Efficiency and Off-design Operating Conditions.

By

Håkan Nilsson and Lars Davidson

Internal Report Nr 01/2,
Thermo and Fluid Dynamics,
Chalmers University of Technology,
Gothenburg,
2001.

Paper IV

An Experimental Investigation of the Flow in the Spiral Casing and Distributor of the Höleforsen Kaplan Turbine Model.

By

Håkan Nilsson, Urban Andersson
and Sebastian Videhult

Internal Report Nr 01/5,
Thermo and Fluid Dynamics,
Chalmers University of Technology,
Gothenburg,
2001.

Paper V

A Numerical Investigation of the Flow in the Wicket Gate and Runner of the Hölleforsen (Turbine 99) Kaplan Turbine Model.

By

Håkan Nilsson and Lars Davidson

Published in the proceedings of the workshop
Turbine 99 - II
June 18-20, 2001,
Älvkarleby, Sweden

Paper VI

**Validations of Finite Volume CFD
Against Detailed Velocity and
Pressure Measurements in
Water Turbine Runner Flow**

By

Håkan Nilsson and Lars Davidson

Submitted for journal publication, 2002

Paper VII

Application of a Momentum-Imbalance Method for Investigating Numerical Accuracy in Swirling Flow.

By

Håkan Nilsson and Lars Davidson

Submitted for journal publication, 2002

Paper VIII

Validations and Investigations of the Computed Flow in the GAMM Francis Runner and the Hölleforsen Kaplan Runner.

By

Håkan Nilsson and Lars Davidson

Accepted for publication at the
21st IAHR Symposium,
September 9-12, 2002,
Lausanne, Switzerland